

# UNIVERSITÀ DEGLI STUDI DI PADOVA

Dipartimento di Fisica e Astronomia “Galileo Galilei”

Master Degree in Physics

Final Dissertation

Control of drop motion by means of optical patterns imprinted on

Fe:LiNbO<sub>3</sub> crystals

Thesis supervisor

Prof. Giampaolo Mistura

Thesis co-supervisor

Dr. Davide Ferraro

Candidate

Mattia Carneri

Academic Year 2020/2021



# Abstract

Controlling and predicting the mobility of sessile droplets in contact with a solid surface has fundamental implications and technological applications. In the last decade, the use of liquid impregnated surfaces has become the best way to improve the wettability of a substrate and promote the motion of sessile droplets. In this thesis we will couple the realization of a liquid impregnated surface with the photovoltaic effect exhibited by Lithium Niobate crystals to control in an active way the motion of sessile droplets. The resulting method is simple and versatile, enabling the successful manipulation of many consecutive drops having typical volumes of micro-liters, without the need for electrodes or power supplies. In particular, the pattern of illumination arriving on the Lithium Niobate is generated by a spatial light modulator which permits to write any shape to control the droplet. After a preliminary exploration of the dynamics of the system, the main goal of this thesis work consists in finding the best parameters to realize and control the motion of a train of droplets in a reproducible way.





# Summary

<b>Introduction</b>	<b>1</b>
<b>1 Wetting</b>	<b>3</b>
1.1 Surface Tension . . . . .	3
1.2 Wetting on Surfaces . . . . .	4
1.3 Drop Dynamics . . . . .	5
1.4 Liquid Infused Surfaces . . . . .	6
1.5 Electrowetting . . . . .	8
<b>2 Lithium Niobate</b>	<b>11</b>
2.1 Chemical Composition . . . . .	11
2.2 Crystal Structure . . . . .	12
2.3 Physical and Optical Properties . . . . .	13
2.3.1 Piezoelectric and pyroelectric effects . . . . .	13
2.3.2 Dielectric permittivity and birefringence . . . . .	13
2.3.3 Electro-optic effect . . . . .	14
2.3.4 Photovoltaic effect . . . . .	14
2.3.5 Photorefractive effect . . . . .	14
2.4 Photovoltaic Effect in Fe:LiNbO <sub>3</sub> . . . . .	15
2.4.1 Drift Current Density . . . . .	16
2.4.2 Photovoltaic Current Density . . . . .	16
2.4.3 Diffusion Current Density . . . . .	16
2.4.4 One-center Charge Transport Model . . . . .	17
2.5 Optowetting on Lithium Niobate . . . . .	18
2.5.1 Photovoltaic Optoelectronic Tweezers . . . . .	18
2.5.2 LIS on Lithium Niobate . . . . .	19
<b>3 Experimental Setup</b>	<b>21</b>
3.1 Optical setup . . . . .	21
3.1.1 Optical Path . . . . .	21
3.1.2 Laser Calibration . . . . .	23
3.1.3 Half-wave plate calibration . . . . .	24
3.1.4 Spatial Light Modulator . . . . .	25
3.2 Sample movement and acquisition system . . . . .	27
3.3 Droplets generation . . . . .	28
3.4 LIS Characterization . . . . .	29
3.4.1 Teflon Filter . . . . .	29
3.4.2 Sliding Measurements . . . . .	29
3.4.3 LIS on Lithium Niobate . . . . .	31
<b>4 Experimental Results</b>	<b>35</b>
4.1 Intermittent Illumination . . . . .	36

4.1.1	Pendant Drops Fall Height . . . . .	36
4.1.2	Velocity of droplets on the illuminated pattern . . . . .	38
4.1.3	Natural Discharge of Lithium Niobate . . . . .	39
4.1.4	Crossed patterns . . . . .	40
4.1.5	Discharge of the Fe:LiNbO <sub>3</sub> induced by the droplets . . . . .	42
4.2	Continuous Illumination . . . . .	43
4.2.1	Velocity of droplets on the illuminated pattern . . . . .	43
4.2.2	Train of droplets . . . . .	44
4.2.3	Different patterns of illumination . . . . .	47
<b>5</b>	<b>Conclusions</b>	<b>51</b>
	<b>Bibliography</b>	<b>53</b>

# List of Figures

1.1	Surface Tension Scheme . . . . .	4
1.2	Surface Tension Force Balance . . . . .	4
1.3	Wetting Regimes . . . . .	5
1.4	Sessile Droplet Sliding . . . . .	6
1.5	LIS Configurations . . . . .	7
1.6	Electrowetting Scheme . . . . .	9
2.1	Phase diagram of $\text{Li}_2\text{O}-\text{Nb}_2\text{O}_5$ system. . . . .	11
2.2	Crystal Structure of Lithium Niobate . . . . .	12
2.3	Paraelectric and Ferroelectric phases of Lithium Niobate . . . . .	13
2.4	The photorefractive effect stages in Lithium Niobate. . . . .	15
2.5	Transport of photoexcited electrons in photovoltaic effect . . . . .	17
2.6	Dielectrophoretic and Electrophoretic forces simulation . . . . .	19
3.1	A photo of the optical path. . . . .	22
3.2	Scheme of the optical path with all its components. . . . .	23
3.3	Power measured by PowerMax PM10 as a function of $P_{mon}$ . . . . .	24
3.4	Half-wave plate calibration . . . . .	25
3.5	Spatial Light Modulator model . . . . .	26
3.6	Conversion in diffraction optical element of an image by the SLM . . . . .	26
3.7	Photo and scheme of the apparatus near the sample . . . . .	27
3.8	LabView example to analyse the motion of the droplet . . . . .	28
3.9	Syringe pump model and LabView program to control the pump . . . . .	28
3.10	PTFE membrane filter characteristics . . . . .	29
3.11	LIS impregnation stages . . . . .	30
3.12	Capillary vs Bond Number: LIS characterization . . . . .	31
3.13	Lithium Niobate sample plain and with the filter impregnated . . . . .	32
3.14	LIS characterization for different oil height . . . . .	33
4.1	Example and scheme of illuminated pattern generation . . . . .	35
4.2	Height of fall of the pendant drop interacting with the dielectrophoretic force . . . . .	37
4.3	Plot of the height of fall of the pendant drop as a function of the time of exposure . . . . .	38
4.4	Inclination of the illumination pattern vs speed of the droplet (intermittent) . . . . .	39
4.5	Droplets interacting with crossed illumination patterns . . . . .	41
4.6	Inclination of the illumination pattern vs speed of the droplet (continuous) . . . . .	44
4.7	Efficiency of the trains of 50 droplets . . . . .	45
4.8	Efficiency of the trains of 100 droplets . . . . .	46
4.9	Train of 100 droplets: first vs last droplet . . . . .	47
4.10	Curved illumination pattern . . . . .	48
4.11	Broken illumination pattern . . . . .	48
4.12	Undulated illumination pattern . . . . .	49



# Introduction

The control and prediction of the motion of droplets in contact with a solid surface is a major scientific challenge and is crucial for an ample variety of applications [4]. Different methods have been explored to achieve the passive motion control of droplets, many of which inspired by solutions already present in plants, like self-cleaning, slippery or hydro-repellent leaves [7]. For example, the lotus leaves [4], where the droplet is no more interacting with a solid surface but with an air cushion [6], or the *Nepenthes* pitcher plant [8], which has its peristome impregnated with a sweet aqueous liquid that attires insects from outside. The latter has been easily replicated in laboratory as a textured surface where pockets of lubricating liquid can be trapped. This replica is called liquid infused surfaces or lubricant impregnated surfaces (LIS) [5][6] or slippery liquid infused porous surfaces (SLIPS) [7], and is a textured solid material soaked with lyophilic oil. The droplets slide on a liquid surface, which is intrinsically smooth down to the molecular scale, it is incompressible, it can immediately self-repair damaged sites and can repel immiscible liquids of any surface tension. The manipulation and control of droplets can be also achieved in an active way, by introducing an external force on the system. One of the most known techniques is the electrowetting [14]: by placing the droplet between two electrodes and applying an electric voltage, the wettability of the surface can be changed and the motion of the droplet controlled. The evolution of this technique is the electrowetting on a dielectric (EWOD): by the introduction of a thin layer of dielectric between the droplet and the conducting substrate, the variation of electric energy takes place across the dielectric and so the electrolysis of the droplet is prevented. The limitation of the EWOD is that the electrodes have to be fixed and embedded in the substrate, thus the motion of the droplet is hindered by the initial chosen configuration, which cannot be changed. The development of optowetting [26] in the last years found a solution to this problem: the technique exploits the photovoltaic effect induced in a suitable material by light illumination. The charges that are generated on the surface of the substrate change its wettability. In this way the electrodes now are virtual, with a high degree of reconfigurability and can be developed without the presence of metallic devices. In the last years, the most used substrate has been the Lithium Niobate ( $\text{LiNbO}_3$ , LN) [17], which can be exploited for its photovoltaic property that consists in the rising of a stationary current after the crystal is exposed to light. This current generates an electric field which extends outside the substrate. Several studies and simulations [28] were performed to understand that the photoinduced electric field can interact with polar and dielectric particles or droplets on the substrate through an electrophoretic (EP) and a dielectrophoretic (DEP) force. After the results obtained in the last years, the photovoltaic optoelectronic tweezers (PVOT) technique [29] was developed: it exploits the dielectrophoretic and electrophoretic forces to manipulate neutral or charged objects. Recently, PVOT have experienced a remarkable development, succeeding in the manipulation, trapping, and patterning of a large variety of micro- and nano-objects, including particles (metal, dielectric, organic, etc. [23]) and non-polar liquid droplets [24]. The technique is simpler because it operates at low light intensity, the illumination pattern on the substrate can assume different shapes (by combining different optical elements) and the effect of the illumination also does not cease after its shutdown. The goal of this work is to control the motion of sessile water droplets sliding on an inclined plane by coupling the realization of a LIS on a LN sample and the dielectrophoretic force generated by the illumination on the Lithium Niobate. The behaviour of sliding droplets on LIS is tested for different volumes, impregnation oils and tilting angles of the substrate. The resulting dielectrophoretic force due to the photoinduced charge is analyzed by moving a pendant drop with respect to the laser spot

and observing its deformation. Then we explore the dynamics of sliding droplets on LN samples, coated with a LIS, with different types of illumination (intermittent or continuous), different angles of inclination of the luminous pattern, with a saline solution instead of pure water and different shapes of luminous patterns, realized using a spatial light modulator. These preliminary measurements are necessary to establish some parameters to realize the motion control of sessile droplets on LN samples with different conditions. The thesis is structured in four chapters:

- **Chapter 1:** an introduction of the theoretical basis of surface wetting, of dynamics of droplets on an inclined plane, of liquid impregnated surfaces and of electrowetting;
- **Chapter 2:** a brief presentation of the main properties of Lithium Niobate, from the chemical composition and crystalline structure, to the physical and optical characteristics. The photovoltaic effect and the generation of dielectrophoretic forces are described to introduce the optowetting and the photovoltaic optoelectronic tweezers;
- **Chapter 3:** the experimental setup is described, the optical apparatus and spatial light modulator, the apparatus for generating droplets and the fabrication and characterization of liquid impregnated surfaces;
- **Chapter 4:** the experimental results are presented, each one with an introduction regarding the protocol for data collection, and then an analysis and discussion of the experimental data.

# Chapter 1

## Wetting

This chapter is a presentation of the physical properties of liquids at the microscale. In particular it will start explaining the fundamental concepts of wetting, the sliding of droplets on an inclined plane and how this motion can be promoted through the use of Liquid Infused Surfaces and electrowetting.

### 1.1 Surface Tension

A liquid is a condensed state in which there is a mutual attraction among the molecules stronger than the thermal agitation. The liquid surface can be seen as a membrane characterized by a surface tension that opposes distortion [1]. The surface tension derives from the discontinuity of density between two immiscible fluids, and this discontinuity at the interface is a consequence of the unbalance between intermolecular forces between molecules. There are two different states for a molecule: the bulk state and the interfacial state [1], represented in Figure 1.1. The molecules in the bulk state are surrounded isotropically by other molecules, which produce a total attractive energy  $U$ . The molecules at the interface can only interact with half of the molecules "below", so their total energy is  $U/2$ : when a molecule goes from the bulk to the interface it loses  $U/2$  energy. The surface tension  $\gamma = U/2a^2$ , where  $a$  is the characteristic molecular size, is a direct measure of this energy shortfall, from bulk to surface, per unit surface area.

The surface tension can be seen from another point of view[1]: if the surface of the interface is increased of a quantity  $dA$ , the work to apply is proportional to the number of molecules to pull to the surface from the bulk to increase the surface area  $dA$ . The work is also proportional to the interaction between the molecules: the stronger the interaction, the more work to increase the surface area. This is represented by the surface tension  $\gamma$ .

The equation for the work is:

$$\delta W = \gamma \cdot dA \quad (1.1)$$

So the surface tension  $\gamma$  is defined as the energy that must be supplied to increase the surface area by one unit [1].

The surface tension is also linked to the overpressure existing in the interior of drops and bubbles: this jump in pressure across the interface is due to the meniscus curvature and can be summarised through Laplace's law [1]:

$$\Delta p = \gamma \left( \frac{1}{R_1} + \frac{1}{R_2} \right) \quad (1.2)$$

Where  $R_1$  and  $R_2$  are the radii of curvature of the interface.

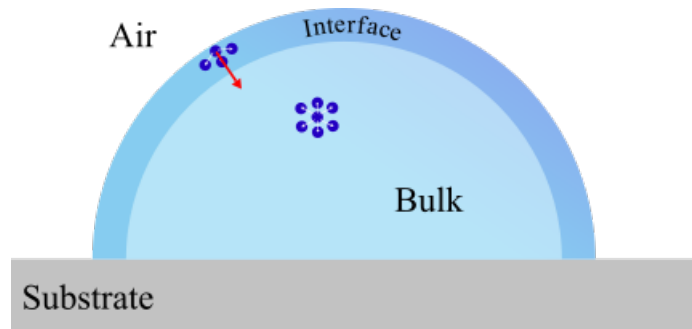


Figure 1.1: Microscopic origin of surface tension: molecules at the liquid/gas interface interact with less neighbours than molecules in the bulk.

## 1.2 Wetting on Surfaces

The study of how liquids spread on a solid surface is called wetting. In this system three interfaces have to be taken into account: liquid-solid, liquid-air and air-solid, as in Figure 1.2. The contact line is the line where the three phases coexist, and it delimits the area wetted by the liquid.

If the system with solid-liquid interaction is considered, there are two different regimes of wetting: complete and incomplete. The parameter to distinguish them is the spreading parameter  $S$ , which is the difference of the energy of the substrate when it is dry and when it is wet:

$$S = E_{\text{substrate}}|_{\text{dry}} - E_{\text{substrate}}|_{\text{wet}} \quad (1.3)$$

or

$$S = \gamma_{SA} - (\gamma_{SL} + \gamma_{LA}) \quad (1.4)$$

where the three parameters are the surface tension at the solid-air, solid-liquid and liquid-air, respectively. If  $S > 0$  the liquid spreads completely on the surface of the solid in order to lower its surface energy (total wetting). If  $S < 0$  the drop does not spread and forms, at equilibrium, a hemispherical cap resting on a surface with a contact angle  $\theta_E$  (incomplete or partial wetting). The contact angle is the result of the mechanical equilibrium among the three surface tensions, which is expressed by Young's equation[3]:

$$\gamma_{LA} \cos \theta_E = \gamma_{SA} - \gamma_{SL} \quad (1.5)$$

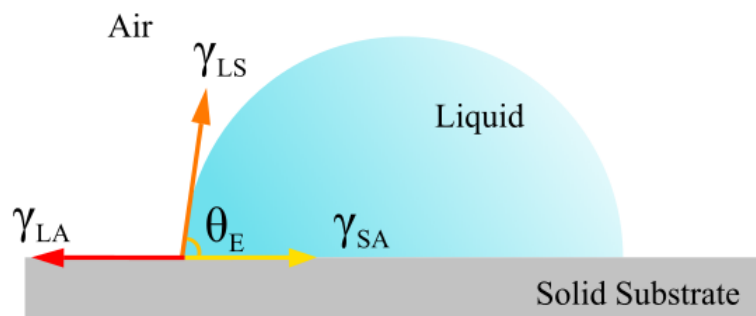


Figure 1.2: Liquid drop on a solid surface with the surface tensions of the three interfaces.

The contact angle can be directly measured by optical imaging, and it is the natural parameter to use to distinguish three classes of surfaces, when a drop of water is put on top of them, like in Figure 1.3:

- hydrophilic surface:  $\theta_E < 90^\circ$ ;
- hydrophobic surface:  $90^\circ < \theta_E < 150^\circ$ ;
- superhydrophobic surface:  $\theta_E > 150^\circ$ ;



The hydrophobic-hydrophilic character of a surface depends on its chemical nature. The superhydrophobicity nature requires also the presence of a rough surface at the micro-nano scale. When the water completely spreads on the substrate it is the case of the complete wetting regime and corresponds to the condition  $\gamma_{LA} \leq \gamma_{SA} - \gamma_{SA}$ .

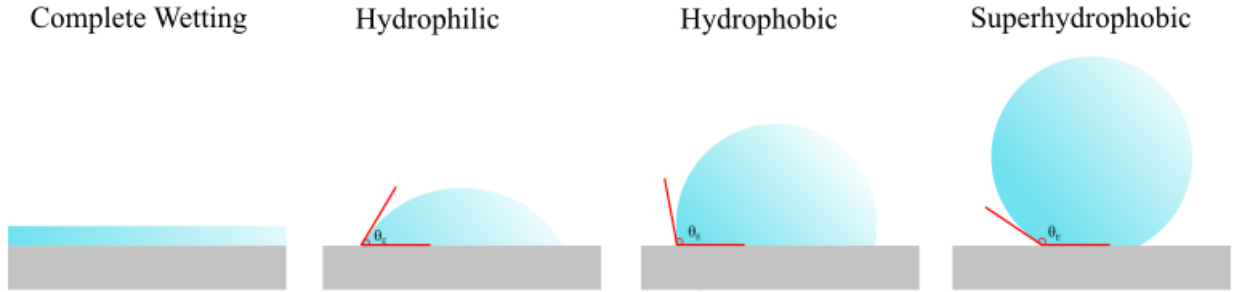


Figure 1.3: Wetting regimes, from left to right: complete wetting, hydrophilic surface, hydrophobic surface, superhydrophobic surface.

### 1.3 Drop Dynamics

In droplet-based microfluidics studies, the goal is to sort, merge and mix droplets to realize chemical or biomedical analyses. Since the system is composed of the substrate and the droplet, the easiest way to better control the motion of the droplet is to modify the interfacial energy and so the wetting properties. In this section the basic concepts linked to drop dynamics will be introduced: the contact angle hysteresis, the introduction of liquid impregnated surfaces and the adimensional numbers to properly analyse the motion of a sessile droplet on an inclined plane.

The equilibrium contact angle  $\theta_E$  is not sufficient to describe the dynamics of a sessile drop on a real surface, due to the presence of morphological or chemical inhomogeneities and defects, which act as pinning sites of the contact line [1]. So it is introduced the contact angle hysteresis:

$$\Delta\theta_H = \theta_A - \theta_R$$

where  $\theta_A$  is the advancing angle and  $\theta_R$  is the receding angle. Their definition is linked to the dynamic behaviour of a droplet on a plane, like in Figure 1.4. The droplet is put on a horizontal substrate and at a certain point the plane is slowly tilted: the shape of the droplet is no more symmetric and the contact angle will increase in the lower part and decrease in the upper part, like in Figure 1.4, until they reach a critical value,  $\theta_A$  and  $\theta_R$ , at which the droplet starts to slide. The corresponding angle of the plane  $\alpha_S$  is called the critical sliding angle. It is clear that the larger is  $\Delta\theta_H$ , the larger is  $\alpha_S$ , so to reduce the droplet-surface friction, the contact angle hysteresis has to be reduced.

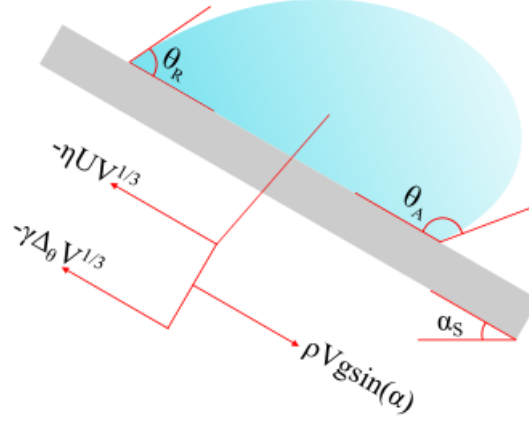


Figure 1.4: Schematic representation of a sessile droplet sliding down an inclined plane, where are highlighted the advancing and receding angle and the balance of forces acting on the droplet.

If the surface is inclined more than  $\alpha_S$ , the drop moving on the surface is subjected to three forces [2], like in Figure 1.4:

- gravitational force  $\sim \rho V g \sin \alpha$ ;
- viscous drag force on the surface  $\sim -\eta U V^{1/3}$ ;
- interfacial force  $\sim -\gamma \Delta_\theta V^{1/3}$ ;

where  $\rho$  is the droplet density,  $V$  its volume,  $\alpha$  the plane inclination,  $U$  the droplet velocity,  $\gamma$  the surface tension and  $\Delta_\theta$  is an adimensional number linked to the distribution of the contact angle around the perimeter of the droplet and to the perimeter of the shape. After the motion is started, the forces will balance and the droplet will reach a constant velocity. A scaling law is obtained from the balance:

$$C_a \simeq B_o - B_{o_c} \quad (1.6)$$

where:

- $C_a = \frac{\eta U}{\gamma}$  is the capillary number which is the ratio between the viscous force versus the surface tension;
- $B_o = \frac{\rho g \sin \alpha V^{2/3}}{\gamma}$  is the Bond number which is the ratio between the gravity component versus the surface tension;
- $B_{o_c}$  is a constant that depends on the contact angle hysteresis through the number  $\Delta_\theta$ ;

The capillary and the Bond number are adimensional, so they are useful quantities to compare systems with different characteristics (like the droplets with different volumes, viscosities, sliding angles, etc.) but same dynamics. They will be used to characterise the LIS that will be used in these experiments like in the article by Smith et al. [6].

## 1.4 Liquid Infused Surfaces

To promote the motion of a sessile droplet on a surface it is necessary to reduce the contact angle hysteresis. Different approaches were followed during the last years, inspired by different plants present in nature with self-cleaning, slippery or hydro-repellent leaves [7]. For example, the lotus leaves [4] [6], where the droplet is no more interacting with a solid surface but with an air cushion, which is trapped inside the roughness of the leave's surface. In this way the friction is significantly reduced. This configuration is called Cassie state: it is not difficult to obtain in the laboratory but it is tricky

to attain robustness of the material over time or under external constraints.

So another inspiration comes from the *Nepenthes* pitcher plant [8] which has its peristome impregnated with a sweet aqueous liquid that attracts insects from outside. If an insect steps on the liquid it is trapped in it and slowly slides inside the plant where the digestive juices are present.

The laboratory's replica consists of a surface where pockets of lubricating liquid can be trapped, instead of an air cushion. These replicas are called liquid infused surfaces or lubricant impregnated surfaces (LIS) [5][6] or slippery liquid infused porous surfaces (SLIPS) [7], and are textured solid materials soaked with lyophilic oil.

The advantages of this kind of configurations are that a liquid surface is intrinsically smooth down to the molecular scale, it is incompressible, it can immediately self-repair damaged sites and can repel immiscible liquids of any surface tension.

The textured surfaces can be produced in the laboratory with different techniques: silicone oil films deposited on a substrate and cooked at high temperature [9], Teflon nanofibrous membranes [7], regular arrays of micro-posts of different shape and parallel grooves using photolithographic techniques [10].

A drop on a LIS is a complicated system since it comprises four different phases: the textured solid, the lubricant, the drop and the surrounding air. The system exhibits 12 thermodynamically stable states, depending on the interfacial tensions, the roughness and the solid fraction [6].

There are 4 relevant configurations that favour a slippery behaviour, i.e. those where the drop does not wet the solid substrate, and are represented in figure 1.5. The drop rests on top of the lubricant (Figure 1.5 (a) and (b)) or sinks into the lubricant and rests on top of the textured substrate (Figure 1.5 (c) and (d)). The lubricant can form a cloak around the drop (Figure 1.5 (a) and (c)), or the drop sinks into the lubricant until the oil forms an annular wetting ridge around it, which pulls the drop above the substrate (Figure 1.5 (b) and (d)). So depending on the material chosen for the drop, the oil and the solid substrate, the LIS can exhibit zero (Figure 1.5 (a)), one or two three-phase contact lines.

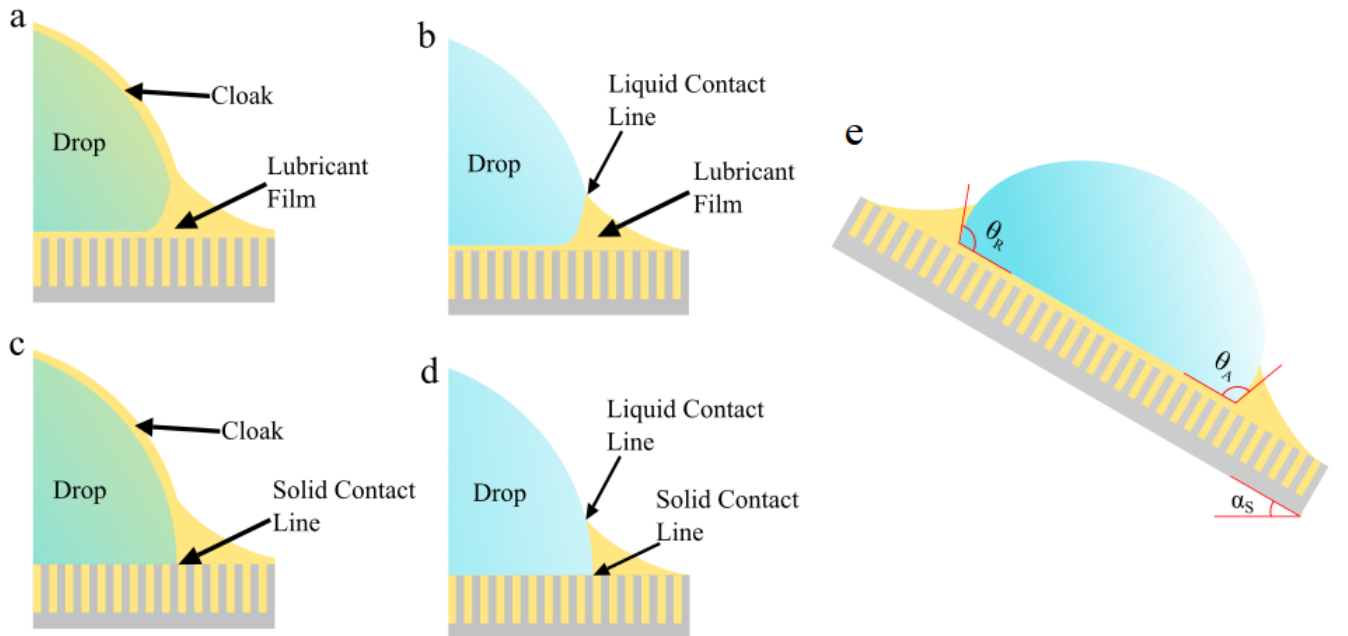


Figure 1.5: Possible wetting configurations of a lubricant-impregnated surface (LIS): (b) and (d) the lubricant does not cloak the drop; (a) and (c) the lubricant cloaks the drop. Drops on LISs can exhibit zero (a), one (b) and (c) or two (d) three-phase contact lines. Finally (e): how the contact angle hysteresis of a sessile droplet on an inclined, is modified by the introduction of a LIS.

The relation between the impregnating oil and the solid substrate is given by the contact angle  $\theta_{os}(a)$

(with o=oil, s=solid and a=air), which has to be less than a critical angle  $\theta_c$  to obtain a stable impregnation. The critical angle is given by:

$$\theta_c = \cos^{-1} \left( \frac{1 - \phi}{r - \phi} \right) \quad (1.7)$$

where  $\phi$  is the fraction of the projected area of the surface that is occupied by the solid and  $r$  is the roughness of the substrate [5].

The top of the texture protrusions can be submerged or exposed depending on the spreading coefficient of the impregnating oil on the solid in the presence of the drop:  $S_{os}(w) = \gamma_{sw} - \gamma_{ow} - \gamma_{os}$ . If  $S_{os} > 0$  a thin film covers the top of textures and eliminates pinning sites. The cloaking mechanism has to be considered since it may prevent condensate growth but also accelerate oil depletion from the solid substrate, and so contaminate droplets.

Cloaking, that is a thin oil film surround the drops, occurs when the spreading coefficient of oil on water surrounded by air,  $S_{ow}(w) = \gamma_{wa} - \gamma_{oa} - \gamma_{ow}$ , is positive. In the case of water drops, cloaking takes place with silicone or fluorinated oils.

There are many different techniques to produce a LIS with various results and the one we used in this work will be described in section 3.4.

The fact that no pinning occurs on LISs makes them ideal surfaces for different applications. For example, water drops can condense on a LIS and their mobility is enhanced because the drops are on a liquid surface with no defect and so minimal pinning. Instead on superhydrophobic surfaces, the condensation occurs within the texture and so the droplet is strongly pinned [4]. Another advantage is that LISs are icephobic [11], can be used for anti-biofouling coatings, instead of chemical attacks or mechanical removal [12].

## 1.5 Electrowetting

Another way to modify the interfacial energy and the wetting properties of the droplet-substrate system is the electrowetting, which has favourable characteristics, like high switching speed, long term reliability and compatibility with various environments. The first observations come from the studies of Lippmann in 1875 on electrocapillarity that were then developed by Berge in the 1990s [13].

The technique consists of the application of a voltage difference between two metallic electrodes in contact through a polar liquid drop. When the voltage is switched on, a local concentration of charges arises in the metallic surface, forming the so-called double charge layer at the solid-liquid interface [14]. In this case, the electrolyte decomposition of the polar solution takes place even when the voltage is of few mV. So Berge introduced the electrowetting on dielectric (EWOD), where a thin insulating layer is put between the droplet and the metallic electrode below. In this case, when the voltage is applied, the wettability of the system is changed due to the electric force developed from the interaction between the polarization charges in the dielectric and the dipole molecules in the polar droplet, like in Figure 1.6.

The global system can be described as two capacitors in series: the dielectric-drop interface, with capacitance  $c_H = \varepsilon_0 \varepsilon_1 / d_h$ , and the metal-dielectric layer, with capacitance  $c_d = \varepsilon_0 \varepsilon_d / d$ , where  $\varepsilon_0$ ,  $\varepsilon_1$  and  $\varepsilon_d$  are the dielectric constants of the vacuum, the droplet and the dielectric,  $d_H$  is the thickness of the double charge layer (few nm) and  $d$  is the thickness of the dielectric. Since  $d_H \ll d$  the total capacitance derives from only one contribution:  $c \approx c_d$ . The effect of the voltage drop inside the droplet on the surface tension is:

$$\gamma_{SL}^{eff} = \gamma_{SL} - \frac{\varepsilon_0 \varepsilon_d}{2d} V^2 \quad (1.8)$$

where the surface tension between the droplet and the dielectric substrate changes due to the presence of the voltage difference  $V$ . From this relation, the Young equation becomes:

$$\cos \theta = \cos \theta_E + \frac{\varepsilon_0 \varepsilon_d}{2d \gamma_{LA}} V^2 \quad (1.9)$$

This relation is valid only at low voltages, beyond a certain threshold the contact angle reaches a saturation value and becomes independent on the applied voltage.

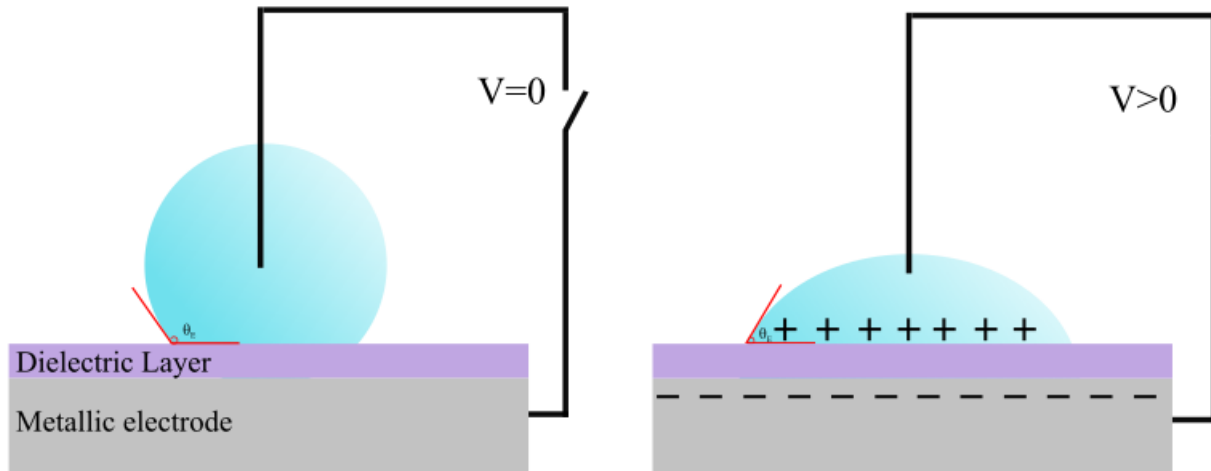


Figure 1.6: Electrowetting setup: partial wetting of the droplet at  $V=0$  (left) and high voltage(right)



## Chapter 2

# Lithium Niobate

The problem with electrowetting is the fact that the metallic electrodes have always to be part of the system and require enwiring to the power supply and cannot be easily reconfigured. To overcome these drawbacks, the Lithium Niobate was considered as a substrate and its peculiar properties exploited. In the following sections, its main characteristics will be briefly explained, in particular how the optowetting can be used to control and manipulate sessile water droplets without the use of physical electrodes.

### 2.1 Chemical Composition

Lithium niobate ( $\text{LiNbO}_3$ , referred also as LN) is a synthetic material made from the  $\text{Li}_2\text{O}-\text{Nb}_2\text{O}_5$  binary system. It is colourless, insoluble in water and in organic solvents, and has excellent chemical stability. It has a high melting point ( $1260^\circ\text{C}$ ), which corresponds to the maximum in the phase diagram, shown in Figure 2.1. The maximum coincides with the congruent composition, i.e. a crystal of LN with a ratio  $\text{Li:Nb}=48.5:51.5$ : it is a Li-deficient structure as compared to the stoichiometric crystals (50:50).

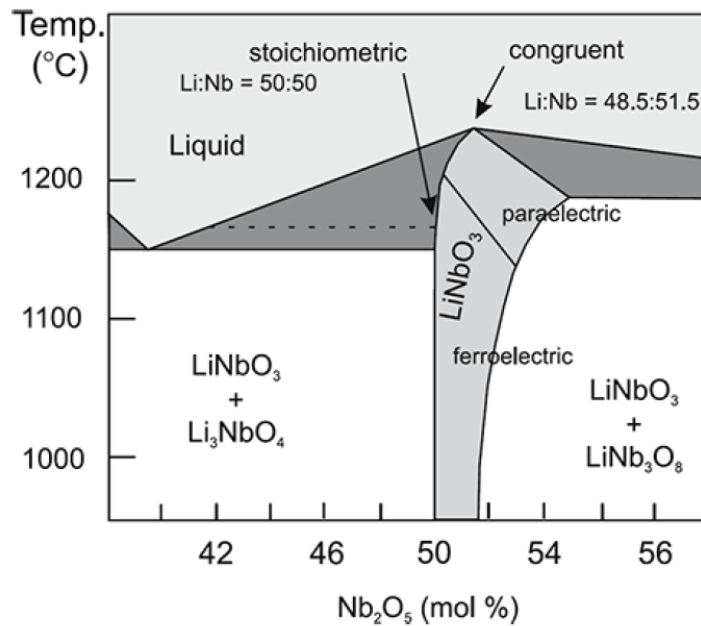


Figure 2.1: Phase diagram of  $\text{Li}_2\text{O}-\text{Nb}_2\text{O}_5$  system.

Since the melted and the solid crystal have the same composition and the Czochralski technique is

used to fabricate the crystal, the final product has a uniform composition and high stability. This is important because the uniformity of the product (the ratio between Li and Nb) can influence many properties of LN, such as the phase transition temperature, the photovoltaic effect and the position of the UV absorption edge [16]. Most commercial products are available in the congruent composition.

## 2.2 Crystal Structure

To describe the structure of the crystal in the trigonal system, three different possible cells can be chosen: hexagonal, rhombohedral and orthohexagonal, represented in Figure 2.2. The preferred choice is orthohexagonal (Figure 2.2 right):

- the  $\hat{z}$  axis corresponds to the optical main axis  $\hat{c}$ , around which the crystal exhibits its three-fold rotation symmetry;
- $\hat{y}$ , laying on one mirror plane;
- $\hat{x}$ , perpendicular to  $\hat{z}$  and  $\hat{y}$ .

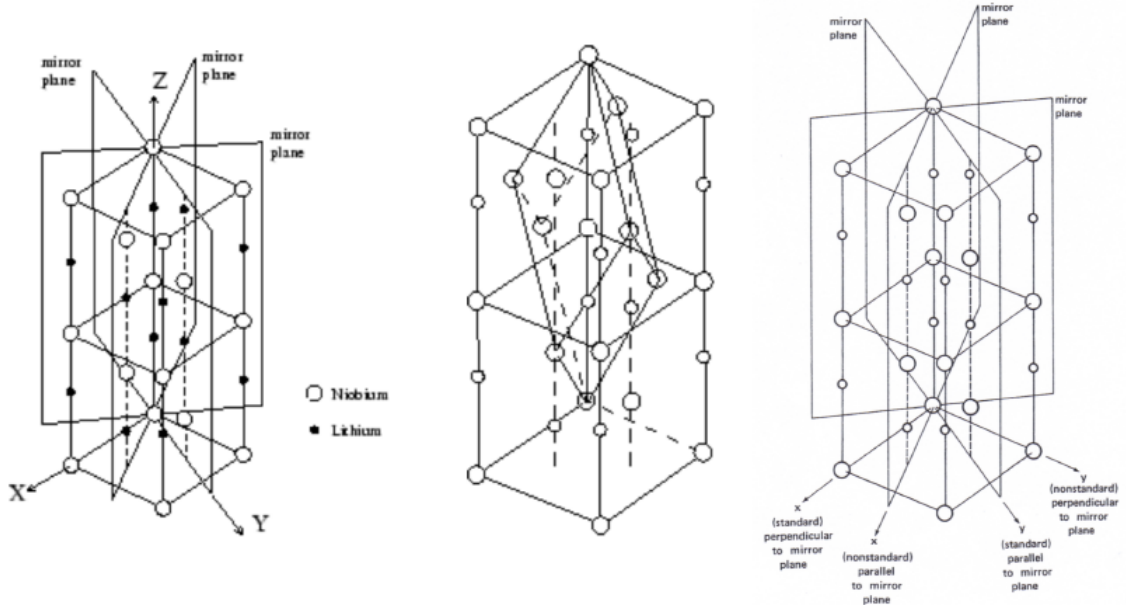


Figure 2.2: Possible crystal structures of LN, from left to right: hexagonal, rhombohedral and orthohexagonal [17].

The positive directions of  $\hat{z}$  and  $\hat{y}$  are the one towards the surface of the crystal which is negatively charged under compression along the relative axes: therefore  $\hat{z}$  and  $\hat{y}$  are piezoelectric directions. The positive direction of  $\hat{z}$  is also the one towards the plane that is positively charged when the crystal is cooled, so  $\hat{z}$  is a pyroelectric direction.

The LN is a ferroelectric material when its temperature is below the Curie temperature ( $T_C \simeq 1210^\circ C$ ): it has a spontaneous polarization that can be reversed when a high external electric field is applied. When the temperature is above  $T_C$  the material is paraelectric [17]. In this case, see Figure 2.3 left, the crystal configuration consists of planar sheets of oxygen atoms along with the  $\hat{c}$  axis, where oxygen coordinates in triangular configurations rotated by approximately  $180^\circ$ ; Li-ions are in the center of the oxygen triangle, while Nb-ions are at the center of an octahedron formed by two triangles.

In the ferroelectric phase, figure 2.3 right, ions move from the previous position along the optical axis  $\hat{c}$  giving rise to non-zero net electrical polarization within the material. The crystal exhibits a mirror symmetry about three planes that are  $60^\circ$  apart. The axis obtained from their intersection is the center of the three-fold rotational symmetry of the crystal. The octahedral interstices between the



oxygen planes are one-third filled by Li atoms, one-third by Nb atoms and the rest is vacant. In the congruent composition, some of the Nb ions can occupy the lattice sites of Li ions.

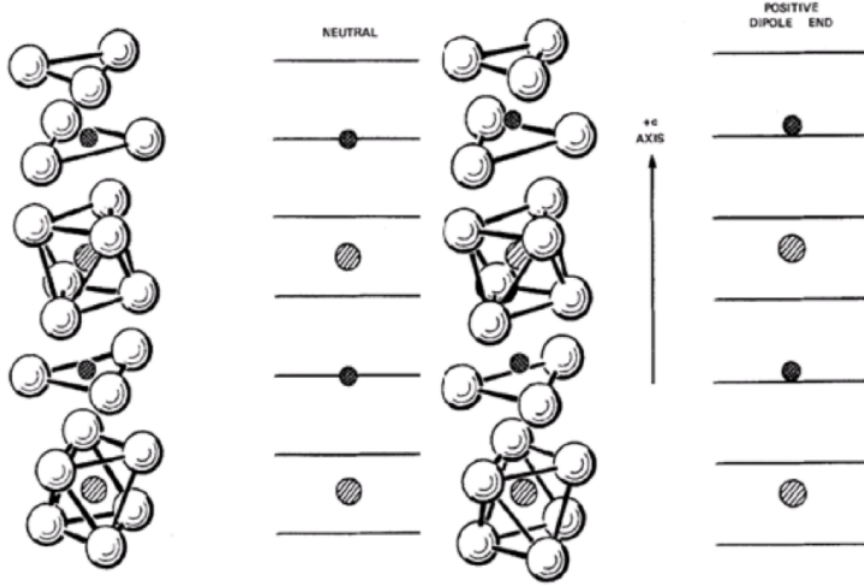


Figure 2.3: Differences between the paraelectric state (left) and the ferroelectric one (right): sketched positions of Li and Nb atoms with respect to the oxygen planes [17].

## 2.3 Physical and Optical Properties

Lithium Niobate is characterised by many physical and optical properties. In the following sections, the main features of the crystal will be presented, in particular the photovoltaic effect.

### 2.3.1 Piezoelectric and pyroelectric effects

Lithium Niobate is a piezoelectric material: when some mechanical compression is applied to it, a polarization is induced, or, conversely, the crystal deforms elastically when a voltage is applied. The polarization induced is given by the formula  $P_z^h = d_h p$ , where  $p$  is the hydrostatic pressure and  $d_h$  is the hydrostatic coefficient ( $d_h = 6.3 \cdot 10^{-12} C/N$  for  $\text{LiNbO}_3$ ) [17].

Lithium Niobate is also pyroelectric: the spontaneous polarization of LN can change due to a variation of temperature. The relation is linear and is given by  $\Delta P = \hat{p} \Delta T$ , where  $\Delta P$  is the variation in the spontaneous polarization,  $\Delta T$  is the variation of temperature and  $\hat{p}$  is the pyroelectric tensor. The change of spontaneous polarization leads to a pyroelectric field:

$$\mathbf{E}_{pyro} = -\frac{1}{\varepsilon \varepsilon_0} \frac{\partial P_s}{\partial T} \Delta T \mathbf{k}_s \quad (2.1)$$

which is proportional to the temperature's change and has antiparallel orientation with respect to the spontaneous polarization direction  $\mathbf{k}_s$ . So the variation of temperature can be used to manipulate micro and nano droplets via the interaction with the generated pyroelectric field through electrophoresis or dielectrophoresis [18].

### 2.3.2 Dielectric permittivity and birefringence

Lithium Niobate is an anisotropic material: the optical response from an external electric field  $\mathbf{E}$  is given by the electric displacement vector  $\mathbf{D} = \hat{\varepsilon} \mathbf{E}$  through the dielectric permittivity tensor  $\hat{\varepsilon}$ . In the

case of LN, with respect to the principal axes, it is:

$$\hat{\varepsilon} = \begin{pmatrix} \varepsilon_{11} & 0 & 0 \\ 0 & \varepsilon_{11} & 0 \\ 0 & 0 & \varepsilon_{33} \end{pmatrix}$$

The ordinary refractive index ( $n_o$ ), which refers to  $\hat{x}$  and  $\hat{y}$  directions, and the extraordinary refractive index ( $n_e$ ), which refers to  $\hat{z}$  direction, are a function of the two coefficients of dielectric permeability:

$$n_o = \sqrt{\frac{\varepsilon_{11}}{\varepsilon_0}} \quad n_e = \sqrt{\frac{\varepsilon_{33}}{\varepsilon_0}}$$

The two refractive indices are different, and this indicates the rise of birefringence [17]. It is also found that the dispersion law depends on the temperature and concentration of Li in the material [20].

### 2.3.3 Electro-optic effect

The electro-optic effect is a second-order optical phenomenon and it is the change of the refractive index in the presence of an high external electric field [19]. This variation can be expressed as power series with respect to the electric field  $\mathbf{E}$ :

$$\Delta \left( \frac{1}{n^2} \right)_{ij} = \sum_k r_{ijk} E_k + \sum_{k,l} s_{ijkl} E_k E_l$$

where the tensors  $r_{ijk}$  and  $s_{ijkl}$  describe the linear (Pockels) and quadratic (Kerr) electro-optic effect. In the case of not very intense electric fields the effect is linear and depends also on the incident light polarization. If the light is polarised along the optical axis  $\hat{c} \equiv \hat{z}$  and propagating along  $\hat{x}$  or  $\hat{y}$ , the variations of the refractive indices are:

$$\Delta n_o = -\frac{1}{2} n_o^3 r_{13} E_z \quad \Delta n_e = -\frac{1}{2} n_e^3 r_{33} E_z$$

and in the case of light polarised along  $\hat{x}$  or  $\hat{y}$  and propagating in  $\hat{z}$  direction:

$$\Delta n_o = -\frac{1}{2} n_o^3 r_{22} E_x \quad \Delta n_e = 0$$

### 2.3.4 Photovoltaic effect

The bulk photovoltaic effect of Lithium Niobate, also known as photogalvanic effect [21], consists of the rising of a stationary current after the crystal is exposed to light. The resultant current is proportional to the intensity of light and to the absorption coefficient of the material, which depends on the light's wavelength. This effect is due to the asymmetry of the energy bands related to ions that constitute the crystalline structure, which causes the photoexcited charge carriers to move in a preferred direction: this current will be described in more detail in section 2.4.

### 2.3.5 Photorefractive effect

The photovoltaic effect and the electro-optic effect both contribute to the photorefractive effect: the refractive index of the LN is modified when exposed to light [22]. This is possible due to the presence of intrinsic and extrinsic impurities with two valence states. They add intermediate levels in-between the valence and conduction band of the pure LN, acting both as donors or acceptors, depending on their valence state. In Figure 2.4 the sequence of the stages of the photorefractive effect are described: a non-uniform light pattern is generated from the interference of a laser beam (a), the crystal is irradiated by the light pattern (b), then the electrons in the illuminated area are excited from the donor level to the conduction band (c), and are transferred inside the material by diffusion, photovoltaic effect or drift phenomena, until they are trapped by acceptors. If the electrons are trapped in the dark

regions (non-illuminated), they can no longer be photoexcited (d). This leads to a non-uniform charge distribution and so to an internal space-charge electric field  $E_{sc}$  (e). The presence of the electric field changes the refractive index of the material through the electro-optic effect and so a refractive index pattern is obtained (f).

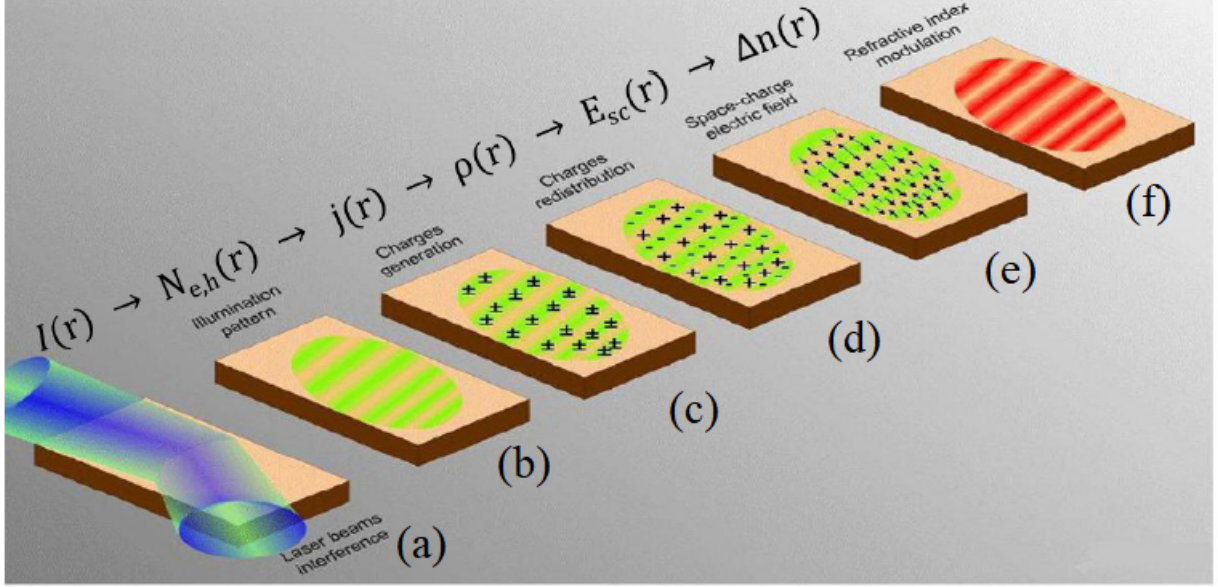


Figure 2.4: The photorefractive effect stages in Lithium Niobate.

In the case of Lithium Niobate, in addition to impurities, also the niobium ions in the valence state  $\text{Nb}_{\text{Li}}^{5+}$  and  $\text{Nb}_{\text{Li}}^{4+}$  play the roles of donors and acceptors respectively. The space charge field due to them is of the order of  $10^4 - 10^5$  V/m. However, if the Lithium Niobate is doped with transition metals, in particular iron, the photorefractive effect is increased up to  $10^6$  V/m. The iron ions act as valence states as  $\text{Fe}^{2+}$  and  $\text{Fe}^{3+}$ : the trivalent ions act as traps for electrons, thus transforming into  $\text{Fe}^{2+}$  ions, which can then be photoexcited, losing an electron and returning  $\text{Fe}^{3+}$  ions.

## 2.4 Photovoltaic Effect in $\text{Fe}:\text{LiNbO}_3$

The photovoltaic effect is the result of charge transport when the Lithium Niobate is exposed to light. In general, the total current density  $\mathbf{j}_{tot}$  inside LN can be seen as a sum of three components: the drift current  $\mathbf{j}_{drift}$ , due to the presence of an external electric field, the photovoltaic current  $\mathbf{j}_{ph}$ , due to the bulk photovoltaic effect, and the diffusion current  $\mathbf{j}_{diff}$ . In summary:

$$\mathbf{j}_{tot} = \mathbf{j}_{drift} + \mathbf{j}_{ph} + \mathbf{j}_{diff} \quad (2.2)$$

which will be briefly described in the next sub-sections. In general, the total current  $\mathbf{j}(\mathbf{r}, t)$  is a function of space and time, and the Poisson equation (2.3) and the continuity equation (2.4) hold for the phenomenon of charge transport:

$$\nabla \cdot (\hat{\epsilon} \mathbf{E}) = \frac{\rho}{\epsilon_0} \quad (2.3)$$

$$\nabla \cdot \mathbf{j} + \frac{\partial \rho}{\partial t} = 0 \quad (2.4)$$

where  $\hat{\epsilon}$  is the dielectric tensor of the material,  $\rho(\mathbf{r}, t)$  is the charge density,  $\epsilon_0$  is the dielectric permittivity in vacuum and  $\mathbf{E}$  is the local electric field.

### 2.4.1 Drift Current Density

The drift current equation represents charges carriers flow induced by with an external electric field, which can be written through Ohm's law:

$$\mathbf{j}_{drift} = \hat{\sigma} \mathbf{E} \quad (2.5)$$

$$\hat{\sigma} = q \mu_{e,h} \hat{N}_{e,h} \quad (2.6)$$

where  $\hat{\sigma}$  is the conductivity tensor,  $q$  the elementary charge,  $\mu_{e,h}$  the mobility tensor and  $N_{e,h}$  the charge carriers density (electrons or holes, depending on the reference band). In the case of LN, the total electric field is the sum of three contributes: the external field  $\mathbf{E}_0$ , the space charge field  $\mathbf{E}_{sc}$ , due to the internal charge distribution, and the pyroelectric field  $\mathbf{E}_{pyro}$ , due to the induced charges because of irradiation. In the case of Fe:LiNbO<sub>3</sub>  $\mathbf{E}_{pyro}$  is completely negligible for light intensities lower than  $10^5 \text{ W/m}^2$ , as in the case of this study.

### 2.4.2 Photovoltaic Current Density

The photovoltaic current density can be written as:

$$j_{ph,i} = \beta_{ijk} e_j e_k^* \quad i, j, k = 1, 2, 3 \quad (2.7)$$

where  $\beta_{ijk} = \beta_{ijk}^*$  is the complex photovoltaic tensor, and  $e_j$  and  $e_k^*$  are the electromagnetic wave versors.

A linearly polarised wave is described by the real part of  $\beta_{ijk}$ , while in a circularly polarised wave also its imaginary part has to be taken into account. In the case of LN, the photovoltaic tensor has four independent non-zero components:  $\beta_{333}$ ,  $\beta_{311} = \beta_{322}$ ,  $\beta_{222} = -\beta_{112} = -\beta_{121} = -\beta_{211}$ ,  $\beta_{113} = \beta_{131}^* = \beta_{232}$ .

As previously mentioned, the photovoltaic current has a preferential direction, that corresponds to the optical axis  $\hat{c}$  ( $\equiv \hat{z}$ ). Along the other directions ( $\hat{x}$  and  $\hat{y}$ ) the current densities are an order of magnitude lower. This is due to the asymmetric energy bands relative to the ions forming the crystal structure of the material.

The current density has a linear dependence with the incidental light intensity:

$$j_{ph} = \alpha k_G I = \frac{\mu \tau_{ph} E_{ph} \alpha}{h\nu} I \quad (2.8)$$

where  $\alpha$  is the absorption coefficient,  $k_G$ , known as Glass constant, describes the anisotropy of charge transport, and is called Glass constant and in the case of Fe:LiNbO<sub>3</sub> is  $2.8 \cdot 10^{-11} \text{ m/V}$ ,  $\mu$  is the charge carriers mobility,  $\tau_{ph}$  is the time within which charge carriers contribute to the transport of photovoltaic charge,  $h\nu$  is the energy of incident photons and  $E_{ph}$  is a phenomenological field used to describe this effect acting on charge carriers.

In particular, for Fe:LiNbO<sub>3</sub> the absorption coefficient depends on the donor ions concentration  $[\text{Fe}^{2+}]$ , hence

$$j_{ph} = k_G \cdot \sigma \cdot [F e^{2+}] \cdot I \quad (2.9)$$

where  $\sigma$  is the absorption cross-section of  $\text{Fe}^{2+}$  ions.

### 2.4.3 Diffusion Current Density

The diffusion current density originates from a charge concentration gradient inside the material:

$$j_{diff} = -q \hat{D} \nabla N_{e,h} \quad \hat{D} = \frac{\hat{\mu}_{e,h} k_B T}{q} \quad (2.10)$$

where  $\hat{D}$  is the diffusion tensor,  $q$  the elementary charge and  $k_B$  the Boltzmann constant.

### 2.4.4 One-center Charge Transport Model

It was previously said that the best way to enhance the photorefractive effect is to dope the LN with Iron, since the new introduced ions  $\text{Fe}^{2+}$  and  $\text{Fe}^{3+}$  act as new donors and acceptors of free charges, like in Figure 2.5.

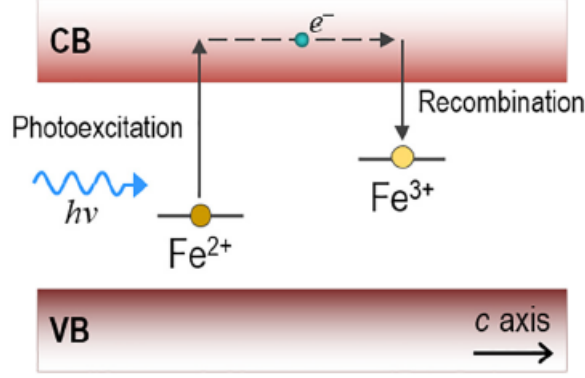


Figure 2.5: The mechanism that regulates the transport of photoexcited electrons in  $\text{Fe}:\text{LiNbO}_3$ .

The mechanism that regulates the transport of photoexcited electrons is fully explained by a set of equations derived by Vinetskii and Kukhtarev (rate equations), in the case of light intensities lower than  $10^6 \text{ W/m}^2$  [16]. The model is based on the assumption that only one kind of ion affects the photovoltaic effect (one-center model): in this case, the dominant contribution arises from Fe dopants. The model can be summarised in the following relations:

$$\frac{\partial N_{e,h}}{\partial t} = (sI + \beta_T)N_{e,h} - \gamma_{e,h}N_{e,h}N_{\text{Fe}^{3+}} - \frac{\nabla \cdot \mathbf{j}}{q} \quad (2.12)$$

$$\frac{\partial N_{\text{Fe}^{2+}}}{\partial t} = -\frac{\partial N_{\text{Fe}^{3+}}}{\partial t} = -(sI + \beta_T)N_{\text{Fe}^{2+}} + \gamma_{e,h}N_{e,h}N_{\text{Fe}^{3+}} \quad (2.13)$$

$$\mathbf{j} = q\mu_{e,h}N_{e,h}\mathbf{E} - qD\nabla N_{e,h} + sN_{\text{Fe}^{2+}}k_G\hat{i} \quad (2.14)$$

where  $\mathbf{j}$  and  $\mathbf{E}$  have the same direction of the optical axis  $\hat{c}$  of the crystal. In this case  $\mathbf{j} \equiv \mathbf{j}_{tot}$ , and  $\mathbf{E}$  to the sum of the external component  $\mathbf{E}_0$  and the space charge field  $\mathbf{E}_{sc}$ , neglecting the pyroelectric component.  $N_{e,h}$  is the charge carriers density,  $s$  is the photon absorption cross-section,  $\gamma_{e,h}$  is the recombination constant,  $\mu_{e,h}$  is the charge mobility,  $D$  the diffusion constant,  $\beta_T$  the thermal generation rate and  $N_{\text{Fe}^{2+}}$  and  $N_{\text{Fe}^{3+}}$  are donors and acceptors concentration respectively. So the Poisson equation and the continuity equation can be rewritten as:

$$\nabla \cdot (\hat{\epsilon}\epsilon_0\mathbf{E}_{sc}) = \rho = q(N_{e,h} + N_{\text{Fe}^{2+}} - N_{\text{Fe}^{2+}}(0)) \quad (2.15)$$

$$\nabla \cdot \mathbf{j} = -q\frac{\partial(N_{e,h} + N_{\text{Fe}^{2+}})}{\partial t} \quad (2.16)$$

where  $N_{\text{Fe}^{2+}}(0)$  is the initial donor concentration without luminous excitation.

Since  $N_{e,h} \ll N_{\text{Fe}^{2+}}$ , in equation (2.15)  $N_{e,h}$  can be neglected. In the second equation the derivative of  $N_{e,h}$  can also be neglected following the adiabatic approximation: the value of  $N_{e,h}$  reaches a stationary state almost immediately (ps) after the light arrives to the LN, and so the value of  $N_{e,h}$  is constant. It also holds for  $N_{\text{Fe}^{2+}}$ . So from equation (2.13):

$$N_{e,h}(\mathbf{r}, t) = \frac{(sI + \beta_T) N_{\text{Fe}^{2+}}(\mathbf{r}, t)}{\gamma} \frac{N_{\text{Fe}^{2+}}(\mathbf{r}, t)}{N_{\text{Fe}^{3+}}(\mathbf{r}, t)} \quad (2.17)$$

It is possible to substitute the result in equation (2.6), to obtain:

$$\sigma = q\mu \frac{sI N_{Fe^{2+}}}{\gamma N_{Fe^{3+}}} + q\mu \frac{\beta_T N_{Fe^{2+}}}{\gamma N_{Fe^{3+}}} = \sigma_{ph} + \sigma_{dark} \quad (2.18)$$

The conductivity is the sum of two different contributes: the photoconductivity  $\sigma_{phi}$ , proportional to the light intensity and the dark conductivity  $\sigma_{dark}$ , due to the thermal excitation of charge carriers when no external radiation is present. Both terms depend on the ratio between the donors and acceptors concentration R:

$$R = \frac{N_{Fe^{2+}}}{N_{Fe^{3+}}} = \frac{[Fe^{2+}]}{[Fe^{3+}]} \quad (2.19)$$

For light intensities greater than 1 W/cm<sup>2</sup>, at room temperature, the thermal excitation is negligible.

## 2.5 Optowetting on Lithium Niobate

The use of electrowetting effect to manipulate droplets is hindered by the constant presence of the metallic electrodes to modify the interface energy between the substrate and the droplet. To overcome this constraint the Lithium Niobate was investigated as an active substrate. In the previous sections its properties have been described, including the photorefractive effect, which can be exploited to manipulate particles and, in particular, droplets through the generation of the dielectrophoretic force.

### 2.5.1 Photovoltaic Optoelectronic Tweezers

In the last decade, the photovoltaic optoelectronic tweezers (PVOT) have been introduced. They are simpler because they operate at low light intensity without electrodes or power supplies. Recently, PVOT have experienced a remarkable development, succeeding in the manipulation, trapping, and patterning of a large variety of micro- and nano-objects, including particles (metal, dielectric, organic, etc. [23]) and non-polar liquid droplets [24]. They are based on the bulk photovoltaic effect, which allows the light-induced generation of very high electric field patterns (100–200 kV/cm) inside certain ferroelectric crystals, such as Fe:LiNbO<sub>3</sub>, which has high availability, high optical quality and can produce high and localised electric fields through the internal polarization and the photovoltaic effect. The photovoltaic field in PVOT remains after the illumination ceases and the technique shows excellent reconfiguration capabilities [25]. These photoinduced electric fields extend outside the active optical material [26] [27] and are able to manipulate micro- and nano-objects, through dielectrophoretic forces (DEP) acting on neutral objects, or electrophoretic forces (EP) acting on charged objects [23]. The expression of EP and DEP forces on a spherical particle are:

$$\mathbf{F}_{EP} = q\mathbf{E} \quad \mathbf{F}_{DEP} = (\mathbf{p} \cdot \nabla)\mathbf{E} \quad (2.20)$$

where  $\mathbf{p}$  is the dipolar momentum of the object induced by the evanescent field  $\mathbf{E}$ . Due to the crystalline and/or geometrical anisotropy of objects, the dipolar momentum induced by the electric field obeys a tensor expression,  $p_{ij} = \alpha_{p,ij}E_j$ , where  $\alpha_{p,ij}$  is the polarizability tensor. Under non-oscillating electric fields (as in the case of PV fields) and for the case of spherical particles, the polarizability becomes a scalar  $\alpha_p$  that can be written as [27]:

$$\alpha_p = 2\pi r^3 \varepsilon_m \frac{\sigma_p - \sigma_m}{\sigma_p + 2\sigma_m} \quad (2.21)$$

where  $r$  is the radius of the particle or droplet;  $\varepsilon_m$  is the absolute dielectric permittivity of the host medium, and  $\sigma_m$  and  $\sigma_p$  are the conductivities of the host medium and particle, respectively. This formula leads to the equation of the dielectrophoretic force:

$$\mathbf{F}_{DEP} = \alpha_p \nabla(E^2) \quad (2.22)$$

so the  $\mathbf{F}_{DEP}$  depends on  $\alpha_p$  sign: when  $\sigma_p > \sigma_m$  the force is attractive, that is it traps particles where the electric field is maximum, while when  $\sigma_p < \sigma_m$  the force is repulsive. Accordingly, the choice of the materials composing the system is fundamental to create a Dielectrophoretic Trap: a position where the force brings back the particles there.

In the article of Carrascosa et al. [28], a model for the charge distribution on a z-cut crystal (or c-cut, where the optical axis is perpendicular to the illuminated surface), which is used in this experiment, has been proposed by performing a simulation through the rate equations, which govern the photorefractive effect in LN crystals, to determine the forces acting on polar and neutral objects above the illuminated surface. The evanescent field outside the LN crystal can be distinguished in: electrophoretic field (EP), which interacts with polar particles/liquids, and dielectrophoretic field (DEP), which interacts with neutral particles/liquids.

In Figure 2.6, it is shown the results of the simulation of EP and DEP forces outside a z-cut crystal, illuminated with a single spot with homogeneous intensity and well defined borders.

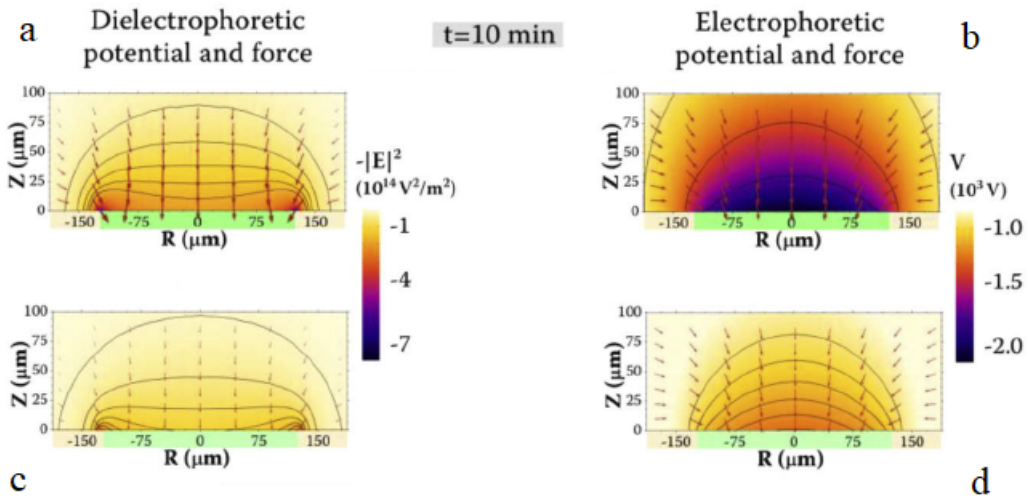


Figure 2.6: (a-c) Dielectrophoretic and (b-d) electrophoretic forces and potentials produced by a circular light distribution. The arrows point towards the local direction of the (a-c) DEP or (b-d) EP force. The upper part corresponds to the illuminated face and the lower one to the non-illuminated one.

As it is shown in Figure 2.6 (a-c), the dielectrophoretic force is maximum at the borders of the illumination spot and minimum in the center and is perpendicular to the surface above the illuminated area, while, from (b-d), the electrophoretic force is maximum in the center of the spot and minimum at the borders. Since the crystal is z-cut, the forces have a radial symmetry around the center of the light beam. The crystal is not at saturation and so the illuminated face (a-b) and the non-illuminated face (c-d) develop DEP and EP forces with different magnitude. An experimental validation of these calculation was given by Puerto et al. [29]: in their experiment a water droplet is suspended on a paraffin oil film, with a certain thickness, on top of a z-cut LN sample. When the droplet is far from the light spot, the DEP force has a small horizontal component that pushes the droplet along the interface toward the illuminated region. However, when the droplet approaches the spot, the vertical component of the DEP force increases and the droplet is attracted by the LN, until it dips in the oil and comes into contact with the LN. It has been observed that the droplet changes its shape and places itself at the border of the illumination spot, where the maximum of the DEP force is located.

## 2.5.2 LIS on Lithium Niobate

The problem with PVOT is the manipulation of objects inside polar liquids, due to electric field screening effects. The solution proposed by Puerto et al. [29] is to cover the LN substrate with a layer of paraffin oil (1-2 mm thickness), on which a water droplet is suspended thanks to a particular configuration that balances the surface tension of oil, droplet and air. In this case the LN substrate

is illuminated by a Gaussian spot that generates the photovoltaic effect and so the dielectrophoretic force acting on the droplet, which is attracted by the illuminated zone. If the water droplet makes contact with the LN substrate, the contact angle of the droplet is modified but it cannot be moved from the contact point.

In our work the LN substrate is covered with a PTFE filter impregnated with a fluorinated oil (see sec. 3.4), making a liquid impregnated surface. In this way the layer of oil is thinner ( $\simeq 1\mu m$ ) but the droplet still does not make contact with the LN. At the same time, the presence of the lubricant film guarantees low friction of the moving droplets. The effect of the dielectrophoretic force on the droplet can be exploited to control the motion of it. So we can use the gravitational force to move the droplet on the inclined plane and the dielectrophoretic force of the illuminated pattern, in this case a simple inclined rectangle, to control this motion.



## Chapter 3

# Experimental Setup

In this chapter the entire setup used for testing the sliding of droplets on illuminated Fe:LiNbO<sub>3</sub> samples is presented. A detailed description is given of the laser beam path and the half-wave plate to control the power arriving on the sample. The software used to control the position of the sample and for data acquisition and processing are presented. Finally the substrate where the droplets are sliding will be characterized.

### 3.1 Optical setup

In this paragraph the setup for optical measurements is presented, as well as all the components that are fundamental to control the shape and the power of the laser arriving on the sample.

#### 3.1.1 Optical Path

The optical path is shown in Figure 3.1 and is composed by:

- five mirrors to control the light;
- a half-wave plate mounted on a motorized goniometer;
- a beam-splitter (PBS);
- a beam expander, composed by two lenses of focal length 25.4 mm (L1) and 150 mm (L2);
- a spatial light modulator (SLM);
- a lens, with focal length 100 mm (L3), to focus the light pattern on a point on a slide to eliminate the zero order of the diffraction;
- a lens, with focal length 100 mm (L4), to focus the pattern on the LN sample;
- a dichroic mirror, that reflects the red light coming from the sample to the camera;
- a red light led that illuminates the sample.

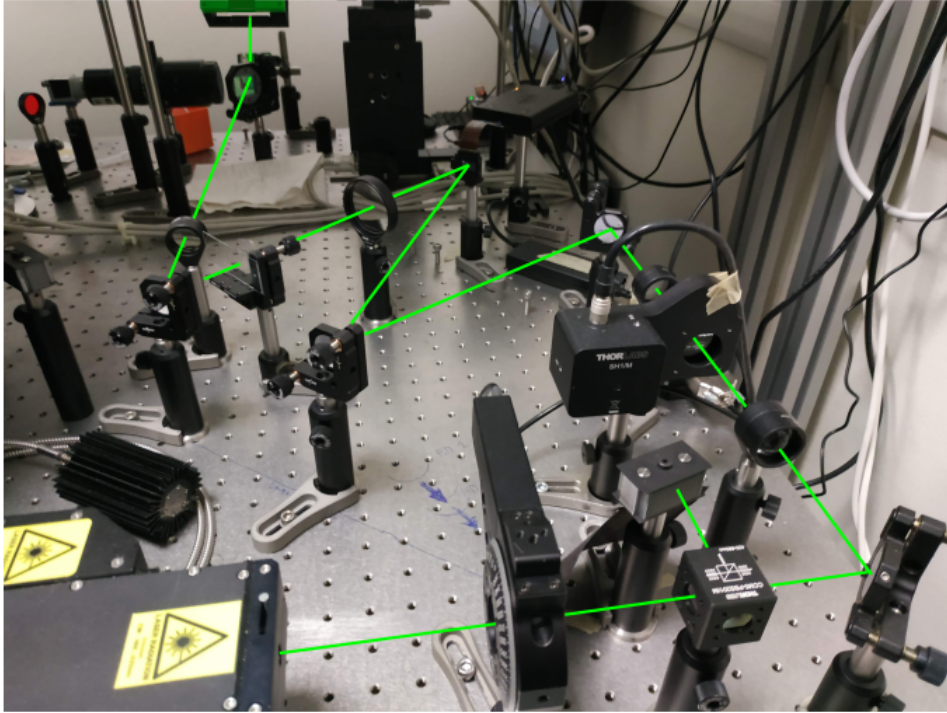


Figure 3.1: A photo of the optical path.

The laser beam is emitted continuously by a solid-state, high power Laser Diode Pump CW connected to an optic fiber amplifier (ALS-GR-532-1-I-SF). The laser beam is gaussian and has a wavelength of 532 nm, with a diameter of 1.5 mm and can reach a maximum nominal power of 1 W. A scheme of the optical path is described in Figure 3.2: right after the laser output, the beam arrives to a half-wave plate mounted on a mechanical goniometer and coupled with a beam splitter. After them, only the horizontally polarized light reaches the first mirror (M1) and arrives at the beam expander: this is composed of two lenses put in sequence, the first (L1) is diverging and expands the initial diameter (1.5 mm) of the beam. The second lens (L2), which is converging, makes the beam collimated with a diameter of 8 mm. Between them the shutter is positioned. The light then hits the second and the third mirrors (M2 and M3) and arrives at the SLM. Then the modulated light passes through the third lens (L3) which focuses the zero order diffraction on the point drawn on the slid. The light then hits the fourth mirror (M4) and passes through the last lens (L4). Before hitting the sample, the beam passes through a dichroic mirror: this mirror lets the green radiation pass but reflects the red light coming from the sample due to the red led, so what is happening on the sample can be recorded by the Basler camera on the left of the dichroic mirror. The beam then it is reflected vertically by the last mirror (M5) and hits the Fe:LiNbO<sub>3</sub> sample.

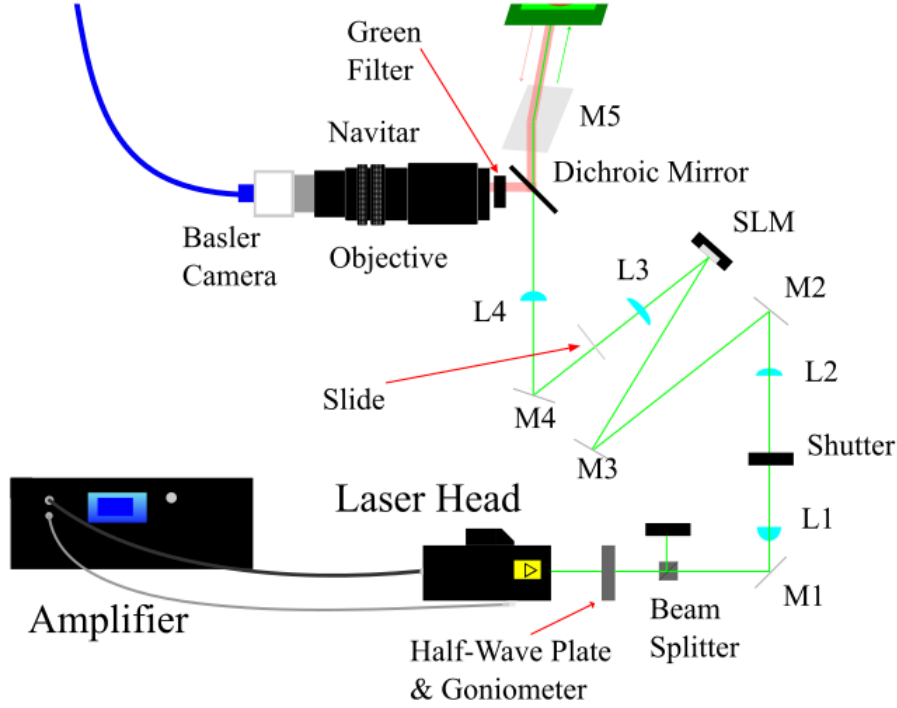


Figure 3.2: Scheme of the optical path with all its components.

The shutter is driven by a controller, which is simply activated by pressing a button. The controller is also connected to an Arduino unit and from the dedicated computer software, APRM, the shutter can be controlled through simple scripts. For example it can be programmed to open the shutter, wait for a certain period of time and then close it: it is useful if we want to expose the sample of Lithium Niobate to the light for a certain period of time.

### 3.1.2 Laser Calibration

The power indicated on the screen of the laser amplifier is nominal, so a measurement of the actual power of the laser beam was performed through the power meter FieldMaxII-TO mounting a PowerMax P10 head. The head was put right after the laser output. In Figure 3.3, the power value measured on the power meter is a function of the voltage  $P_{mon}$  on the monitor: this voltage is linked to the nominal power indicated on the screen but is more precise since it has 3 significant digits.  $P_{mon}$  is used as a reference in all the experiments to be sure to operate every time at the same output power.

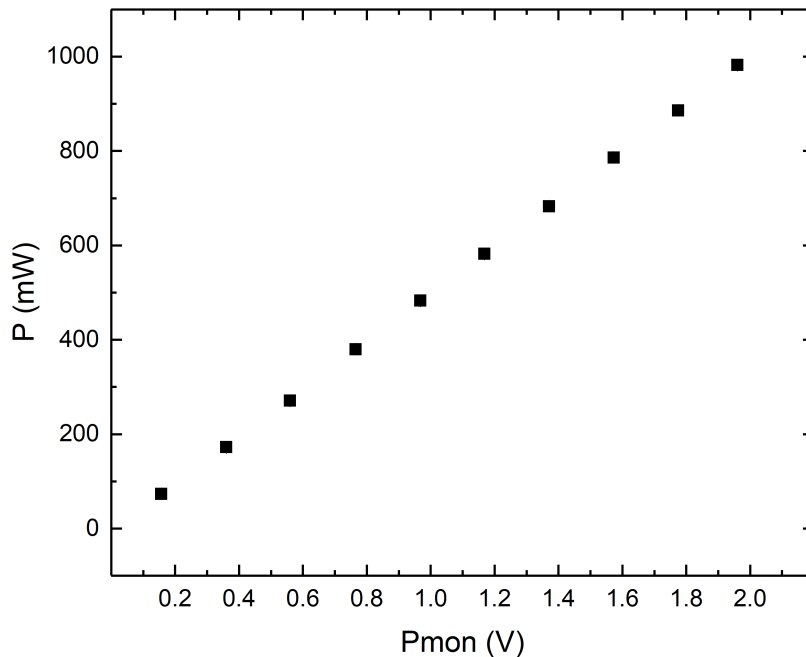


Figure 3.3: Power measured by PowerMax PM10 as a function of  $P_{mon}$ .

### 3.1.3 Half-wave plate calibration

A waveplate, or retarder is an optical device that modifies the polarization state of a light wave travelling through it. The waveplate used in this work is a half-wave plate, which shifts the polarization direction of linearly polarized light. Waveplates are constructed out of a refracting material (plastic), for which the index of refraction is different for light linearly polarized, according to the direction of polarization. The behavior of a waveplate depends on its thickness, the wavelength of light, and the variation of the index of refraction. By appropriate choice of the relationship between these parameters, it is possible to introduce a controlled phase shift between the two polarization components of a light wave, so altering its polarization.

In this experiment the half-wave plate is mounted on a motorized goniometer PRM1Z8 coupled with the KDC101 DC Servo Controller: it can rotate continuously for  $360^\circ$ , with a maximum speed of  $25^\circ/\text{s}$ , and a minimum displacement of  $25$  arcsec. The rotation can be controlled from the dedicated software Kinesis installed on the computer.

The half-wave plate is coupled with a beam splitter: this optical element transmits only the light polarized horizontally and reflects the one polarized vertically into an optical absorber. So the power of the laser beam going out from the beam splitter can be controlled by the rotation of the half-wave plate, since it follows the Malus law:

$$P_{meas} = P_0 - P_{max} \sin^2(2\theta) \quad (3.1)$$

where  $P_{meas}$  is the power measured,  $P_{max}$  is the maximum power measured,  $P_0$  is the power when the waveplate is at  $0^\circ$ , and  $\theta$  is the angle of the goniometer. In Figure 3.4, it is represented a calibration of the half-wave plate: the power is measured by the power meter FieldMaxII-TO mounting a PowerMax P10 head set right after the beam splitter while the angle of the goniometer changes with steps of  $1^\circ$ . It can be seen that the curve follows the Malus law.

Accordingly, the power can be set at the same value for each experiment and then changed to meet the wanted requirements by using the goniometer. The final power that reaches the sample depends on the losses of the optical path, which are known.

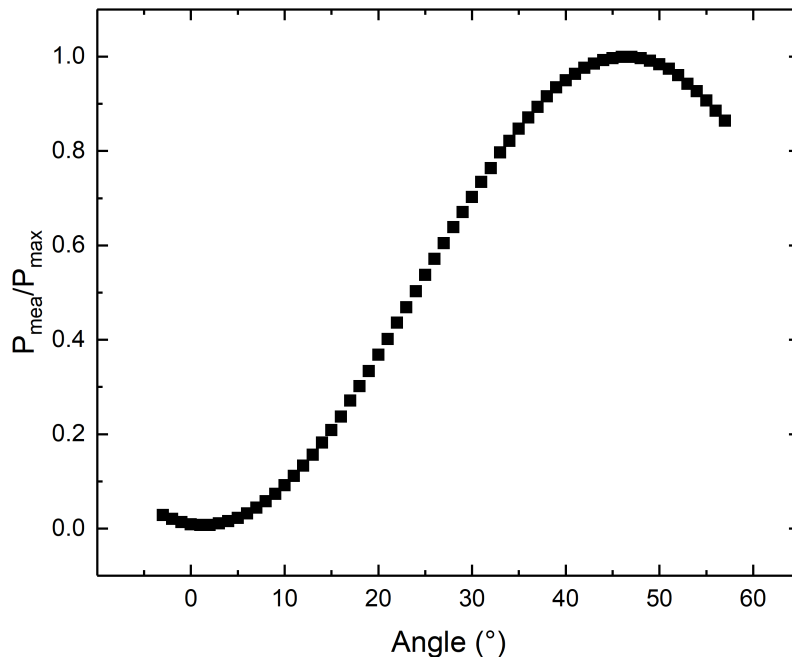


Figure 3.4: The ratio between the power measured versus the maximum power measured as a function of the angle of the goniometer.

### 3.1.4 Spatial Light Modulator

To modify the shape of the laser beam into a design of our choice the LCOS-Spatial Light Modulator was used: it acts on the phase of the incident luminous radiation to preserve the amplitude and the polarization. Thanks to this device it is possible to create different luminous patterns from the collimated laser beam.

The LCOS-SLM (liquid crystal on silicon spatial light modulator) is a spatial light modulator based on liquid crystals on a silicon substrate technology [30]. In this experiment the commercial SLM Pluto-NIR-011 was used, shown in Figure 3.5 (a): it has a display of 15.62 x 8.70 mm with a pixel pitch of 8  $\mu\text{m}$ , a resolution of 1920 x 1080 pixel and an average reflectivity of 65-75%. It is configured for broadband use (from visible to infrared) and it has a fast response time.

It is constituted by two fundamental components: the driver, which controls the electronics and is linked to the computer through a DVI/HDMI cable, and a chip which operates the effective light modulation. The chip has multiple layers: the first one is a silicon substrate, which is implemented by CMOS technology to create a circuit to receive the instructions coming from the driver. The second layer is the upper part of the circuit and is made of aluminium electrodes shaped like pixels, to which is possible to assign an electrical potential independently. The layer between the circuit and a transparent electrode on a slide contains the liquid crystals. These are horizontally aligned, like in Figure 3.5 (b), to manipulate the incoming light which is horizontally polarised. The liquid crystals' molecules can be inclined along a certain direction if a certain electrical voltage is applied to each pixel. This mechanism is used to modify locally the refractive index of the liquid crystals due to their anisotropic optic behaviour: the incoming light passes through the liquid crystals and modifies locally its optical path, and so the shape of the wave front. The information given to the driver are coded in gray-scale (values from 0 to 255) depending on the calibration corresponding to the appropriate wavelength and are used to assign an electrical potential to each pixel.

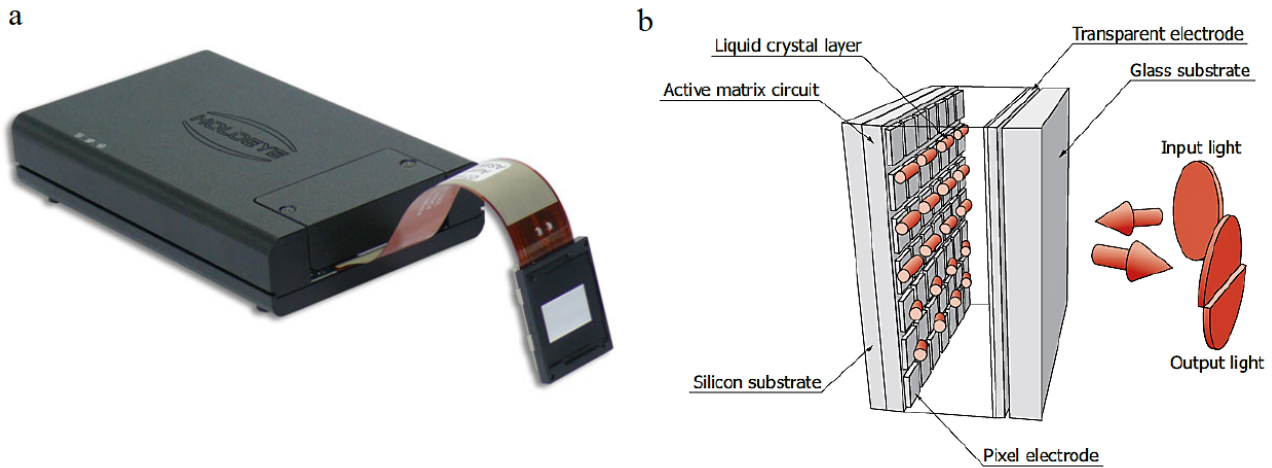


Figure 3.5: (a) SLM Pluto-NIR-011 model used in this experiment; (b) the layers that compose the SLM's display [30].

From the PC interface (HOLOEYE SLM Pattern Generator) it is possible to create phase functions from 8-bit images and send the information to the SLM driver, as shown in Figure 3.6. These phase functions are called diffraction optical element (DOE) or computer generated hologram (CGH) and are calculated by the software. They produce a certain phase function from the input image to obtain its Fourier transform with an intensity distribution of the input image's shape. The DOE is then transmitted to the SLM and so the output wave front will recreate the input image at infinite or in the focal plane of a lens to make it converge. It is also possible to manipulate the output DOE like in the presence of optical objects, such as prisms or lenses: the image can be moved vertically or horizontally, or the focal plane distance can be modified. The structure of the pixels on the display acts like a diffraction lattice which distributes the intensity on different diffraction orders, repeating the same image and so dissipating some of the power in a different direction of the original one.

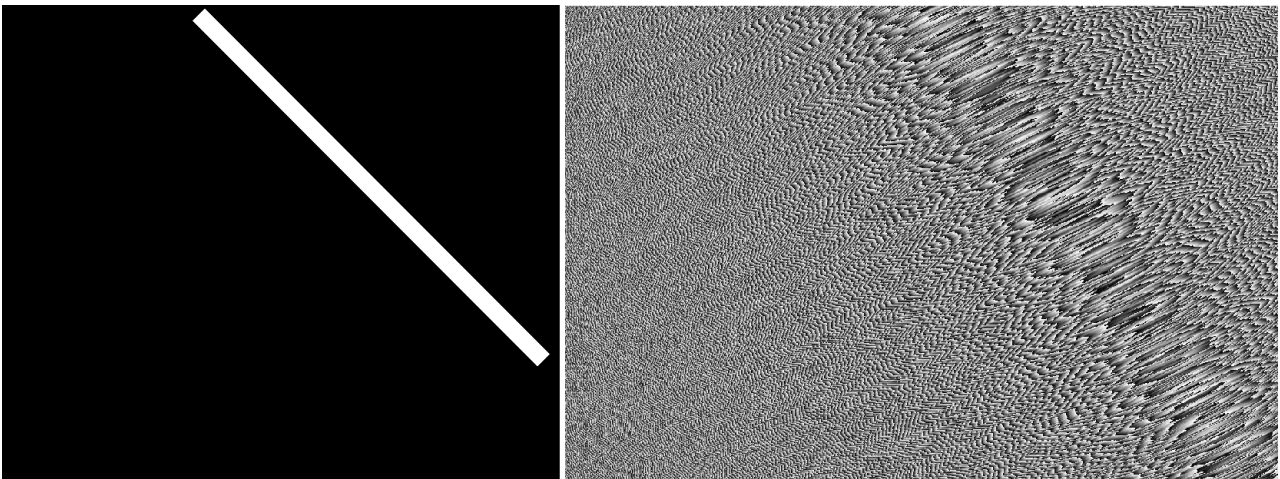


Figure 3.6: Conversion of the original image (left) into its DOE (right)

In order to ensure the best configuration in our setup, three precautions were taken. The input laser beam is expanded to a diameter of around 8 mm to exploit the surface of the SLM display. The SLM, due to the glass on the chip, has a spurious reflection (zero diffraction order) which can not be manipulate through the SLM. So after the SLM there is a lens that focus the spurious reflection on a white spot (made with ink) on a slide. Eventually, in front of the SLM is put a screen (made of black adsorbent paper) with a hole centered on the SLM, to block the higher orders of the diffraction and to let pass only the most intense.



### 3.2 Sample movement and acquisition system

In the apparatus the LN samples are mounted on a sample-holder designed with Catia V5 and printed by Prusa 3D printer. Each sample-holder can be put on handler connected to 3 motorized micrometers, each one aligned to a Cartesian axis (x,y,z) with a range of 25 mm, that can be controlled through a software program (PIMikroMove) from the computer. The angle of the handler can be set through a tilter that can rotate clockwise or counterclockwise at a controlled speed. To verify that the sample is at the correct angle, it is illuminated by a white LED and a CCD camera (MANTA) is used to record the inclination of the sample: the single image is analysed through ImagJ to extrapolate the inclination angle.

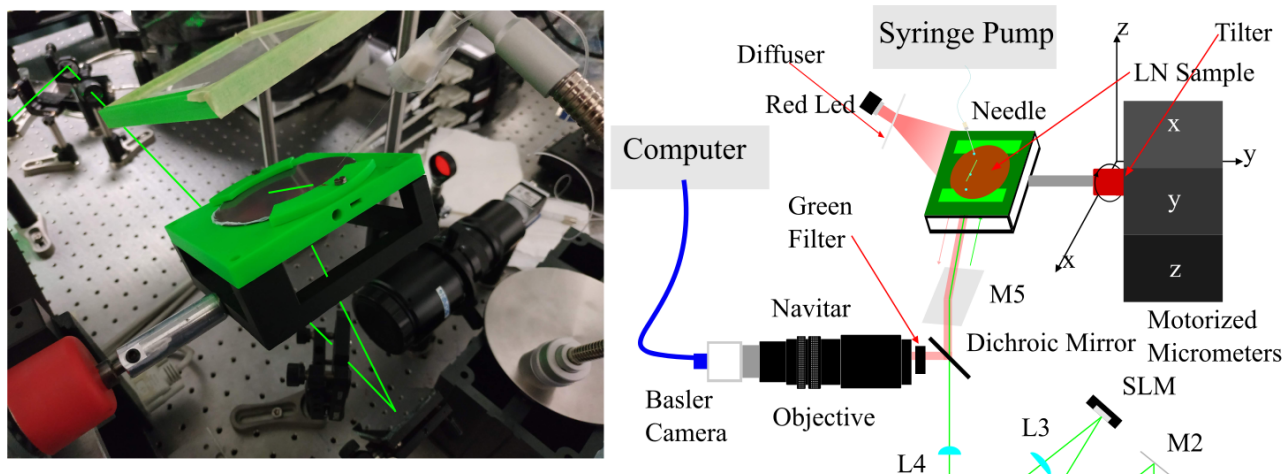


Figure 3.7: On the left a photo of the sample holder as the light hits the sample. On the right a scheme of the setup to control the position of the sample and to record the motion of droplets.

The motion of the droplet on the sample is recorded by a CCD camera Basler acA1300-200um equipped with a Navitar MVL7000 objective. In front of the camera a filter is put to prevent the green light of the laser to hit the objective. The sample is illuminated by a red led with a light diffuser in front of it. It has been chosen red because it does not generate charges on the LN sample. The video of the droplet motion is saved as a sequence of images that can be analyzed through the LabView program shown in Figure 3.8. The program can track the left and right profile of the droplet and so the video can be converted in a series of positions in pixels, which can be converted in millimeters. The motion's law can be extrapolated and so the speed of the droplets.

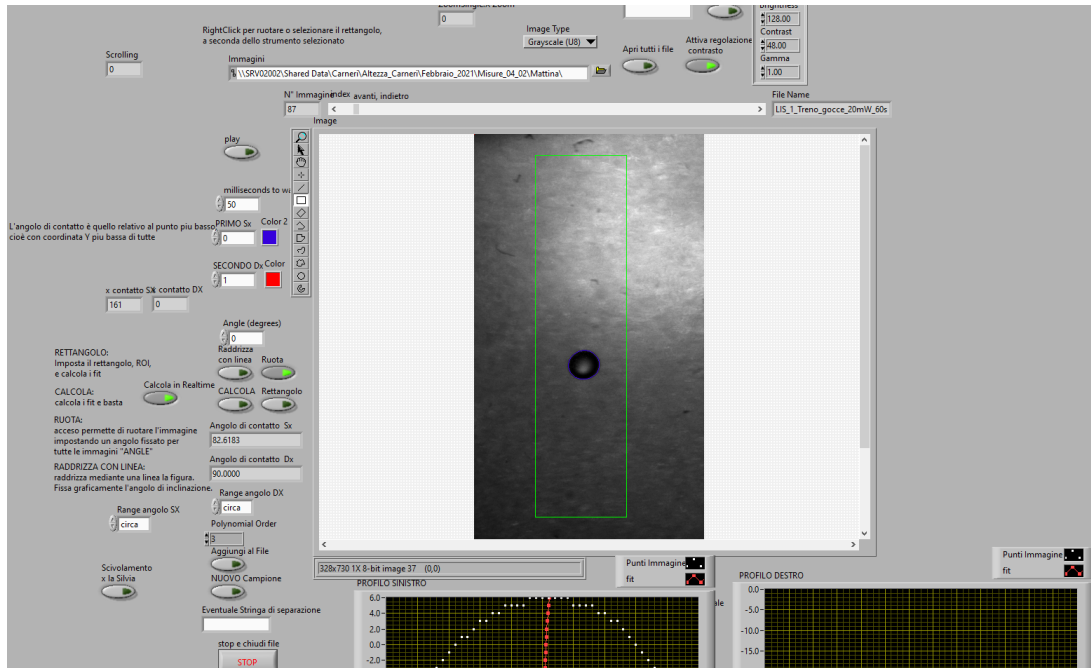


Figure 3.8: LabView program used to analyze the motion of the droplets sliding on the inclined plane. The framing is from the recording from the Basler camera.

### 3.3 Droplets generation

The droplets are generated by the syringe pump PHD 2000: this has a socket where the syringe of 1 mL is placed and it is connected to a PTFE tube of internal radius 0.3 mm and external radius 0.5 mm and ends into a steel needle with external diameter 0.2 mm. The tube is attached to a flexible support that enables the manipulation of the position of the needle in an easy way.

The pump employs a micro-controller which controls a small step angle stepping motor that drives a lead screw. Micro-stepping techniques are employed to further reduce the step angle, eliminating flow pulsation.

The pump can be controlled from the computer by a LabView program: it allows to set the volume of the droplet generated, the speed of generation and to construct simple scripts to repeat the same actions. For example it can generate the droplet, wait a certain amount of time, generate another droplet, and so on. The program can be used to generate a train of droplets with some droplet frequency, which depends on the speed of droplet generation and on the delay set between each droplet generation, which can be both controlled.

The droplets used in these measurements are water hyper pure with resistivity  $\rho = 18.2 \Omega \cdot \text{cm}$ .

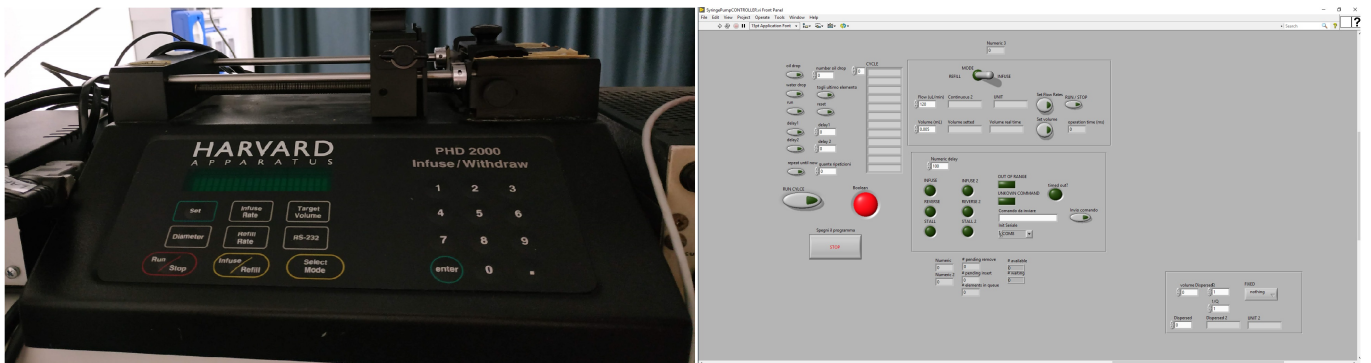


Figure 3.9: On the left: the syringe pump model. On the right the LabView program to control the pump, where the volume, the speed generation of the droplet can be set.



### 3.4 LIS Characterization

In this paragraph, the substrate where the droplets are sliding is presented: from the characteristics of the PTFE filter, to the sliding measurements to determine the best parameters of the LIS used in the measurements.

#### 3.4.1 Teflon Filter

The filter used to produce the liquid impregnated surface is a PTFE membrane, which is hydrophobic and unlaminated. Unlaminated PTFE filters are chemically and biologically inert, stable up to  $260^{\circ}\text{C}$ , and naturally hydrophobic; they are very useful for aerosol sampling, air venting and gas filtration, especially in environments also containing water vapor. These membranes are manufactured through a patented process to form a high-porosity, uniformly thick, thermostable, pure ePTFE structure. The filters were used by Hao et al. [15], to perform electrowetting on a dielectric and were chosen because they exhibit high breakdown voltage.

The average roughness, thickness, and solid fraction of the PTFE membrane are  $\sim 400\text{ nm}$ ,  $\sim 20\mu\text{m}$  and  $\sim 0.16$ , respectively, as measured with a profilometer, as shown in Figure 3.10.

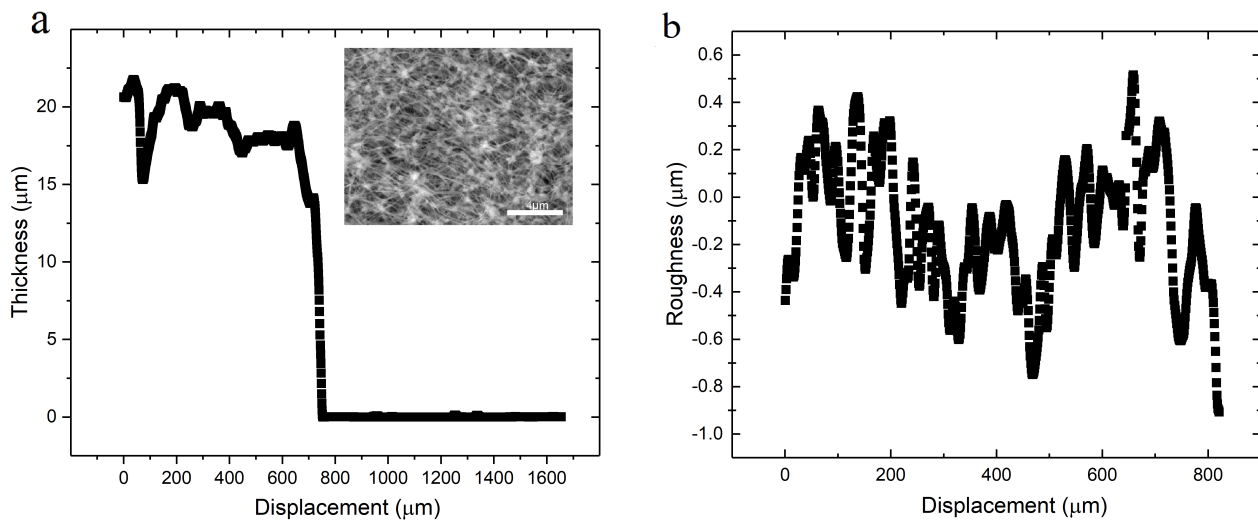


Figure 3.10: PTFE membrane characteristics measured with the profilometer:(a) is the thickness of the membrane, with a picture of the filter taken with the SEM microscope, and (b) is the roughness.

#### 3.4.2 Sliding Measurements

The PTFE membrane was chosen for fabricating the LIS on the Lithium Niobate. This choice is due to the fact that in this way the LN sample does not need to be modified in order to produce the LIS: the filter simply needs to be put on the sample and then impregnated. Before applying the filter on the LN we test its characteristics as a LIS on glass slides: a piece of filter is cut and applied on a clean slide, some ethanol is pipetted on it and when it evaporates, the filter adheres completely on the surface. The filter is then impregnated with some fluorinated oil pipetted on the surface, as shown in Figure 3.13.

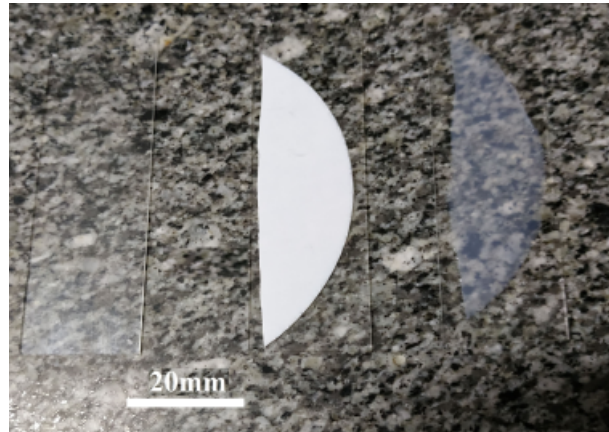


Figure 3.11: From left to right: a clean slide, a piece of PTFE filter applied on the slide and the filter impregnated.

The characteristics of the filter as a LIS are studied by analyzing the dynamics of water droplets sliding on an inclined plane. As we have seen in Section 1.4, it is done through two adimensional numbers: the capillary and the Bond number. These two numbers allow to compare the results of different studies when changing the variables of the experiment. In particular, we can change the volume of the water droplets, the inclination angle of the substrate and the impregnation oil, as listed in Table 3.1.

Oil (viscosity)	Droplets volume ( $\mu\text{L}$ )	Angle
Fomblin Y lvac 06/6 (64 cSt)	0.5, 1, 5, 10, 15	$16^\circ, 23^\circ, 30^\circ, 37^\circ, 45^\circ, 53^\circ, 60^\circ$
FC-40 (2.2 cSt)	0.5, 1, 5, 10	$4^\circ, 10^\circ, 16^\circ$
Krytox (110 cSt)	1, 5, 15	$45^\circ, 53^\circ, 60^\circ$

Table 3.1: Three different oil used to impregnate the LISs, which were studied with different droplets volumes and angles of inclination of the substrate.

When a LIS is ready, we record the motion of 3 droplets sliding on it for each angle and each volume, according to the oil used in the impregnation, and then the measure is repeated for a second LIS with the same impregnation. From the speed of the droplet we obtain the capillary number which is plotted as a function of the Bond number.

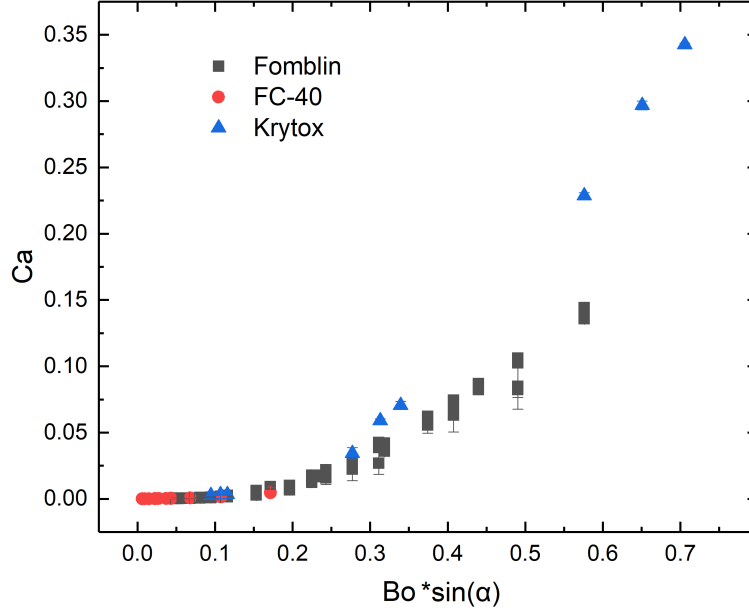


Figure 3.12: Capillary number as a function of the Bond number multiplied by the sine of the inclination angle.

In Figure 3.12, the various measurements for the different oils lie on the same curve, like in the article by Varanasi et al [6]. The FC-40 oil has the lowest viscosity of the three oils and so the droplets slide at low angles and with little volumes (it has similar characteristics of the FC-70, the oil used in the article by Varanasi et al. [6]). The problem with FC-40 is its high vapour pressure, so it evaporates fast ( $\sim$  min) at room temperature, so it is difficult to perform long time measurements, especially when the sample of LN has to be illuminated for different time periods. The Krytox is stable but it is the most viscous and so the droplets have to have high volumes and slide at high angles. Our conclusion is that Fomblin is the best choice. It allows to amply vary both droplets volume and plane inclination to perform the best measurements.

### 3.4.3 LIS on Lithium Niobate

The Lithium Niobate samples used in this experiment are four and are commercial z-cut with doping 0.1 % mol and reduction degree R ( $32.4 \pm 0.5$  %), calculated at 532 nm wavelength. The sample have circular shape with a diameter of 76.2 mm and a thickness of 1mm, like in 3.13 left. To study the filter as a LIS on Lithium Niobate, the operations to apply the filter are the same as the ones seen before, but in this case we chose to use the dip coater to have abetter control on the thickness of the oil above the porous structure of the filter. In the dip coating process, the sample is completely immersed in oil and then it is pulled out with a constant velocity. The height of the oil above the porous surface of the filter depends on this velocity through the law of Landau-Levich [31]:

$$h_0 = c \frac{(\eta U_0)^{2/3}}{\gamma_{LA}^{1/6} (\rho g)^{1/2}} \quad (3.2)$$

where  $\eta$  and  $\rho$  are the viscosity and the density of the oil,  $U_0$  is the velocity of withdrawal of the sample from the oil,  $\gamma_{LA}$  is the surface tension between the oil and air and  $c$  is a constant. After the impregnation each sample of Lithium Niobate will be called "LIS 1", "LIS 2", "LIS 3" and "LIS 4".

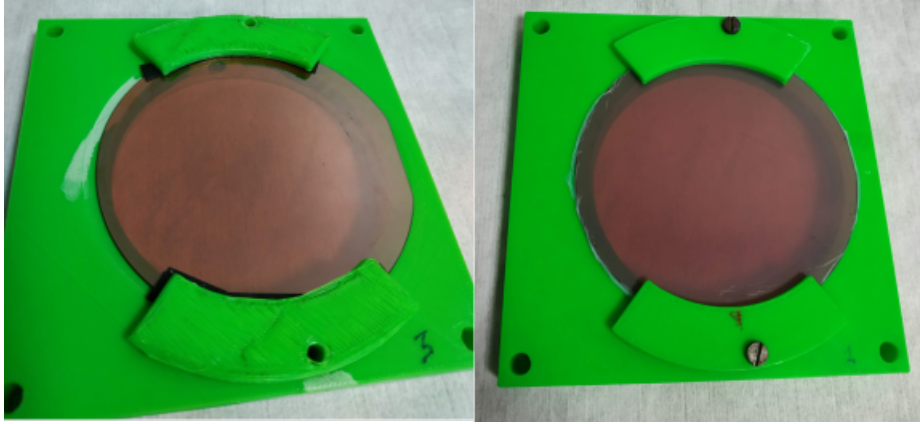


Figure 3.13: Left: a Lithium Niobate sample, right: a Lithium Niobate sample with the filter applied and impregnated with Fomblin Y lvac 06/6.

As stated above, the oil chosen in this experiment is the Fomblin Y lvac 06/6 from the results obtained in the characterization of the filter. Two nominal heights of the oil layer have been tested:  $1\ \mu\text{m}$  and  $0.5\ \mu\text{m}$ , which corresponds to  $0.33\ \text{mm}/\text{min}$  and  $0.12\ \text{mm}/\text{min}$  withdrawal velocities. The height of the oil substrate was chosen to be as smaller as possible to avoid that interaction between the oil and the dielectrophoretic force was stronger than the one with the droplets and to avoid cloaking, but high enough to have a good sliding of the droplet without pinning.

To decide which was the best option to use in the sliding experiments, a stress test was performed. The volume of the droplets and the inclination of the plane are always  $5\ \mu\text{L}$  and  $30^\circ$ . The two values were chosen from the results of the previous tests as a good compromise to have droplets with a velocity high enough to see the difference when the droplet is interacting with the light patterns generated on the LN substrate.

To evaluate the slippery behaviour of LIS with different impregnation height, we have measured the velocity of these trains of droplets. The first height of impregnation to be tested was  $1\ \mu\text{m}$  on LIS 1 and the measurement routine was:

- 20 droplets slide on the oil with a time interval of every 30 seconds;
- the motion of the  $1^{\text{st}}$ ,  $5^{\text{th}}$ ,  $10^{\text{th}}$ ,  $15^{\text{th}}$ , and  $20^{\text{th}}$  is recorded;
- the process is repeated in three different position of the LIS, 10 mm distant.

The routine was repeated several times and between each complete run the LIS was "discharged": water droplets were pipetted on the surface of the LIS and left there for 15 minutes (this is the process used to discharge the sample when illuminated by the laser). It has to be taken into account since the high quantity of water dropped on the LIS can influence the impregnation, and so the motion of the droplet. In Figure 3.14 left, the results of the tests on LIS 1 are summarized: each point represents the average of the droplets velocities for each attempt. The first three runs were done sequentially in the same day, and the last three after 2 days. As we can see the first attempt is not compatible with the others, this is because it is the one right after impregnation and the oil is not well distributed. The second and the last three runs are compatible with a mean velocity around  $6\ \text{mm}/\text{s}$ , which is a bit too low for our experiments.

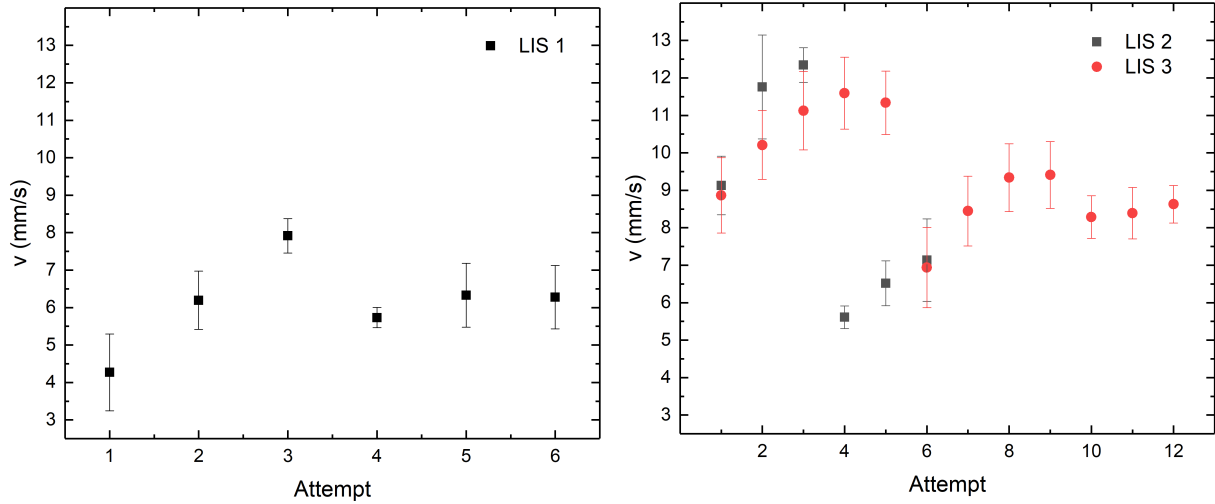


Figure 3.14: Velocity confrontation of droplets of  $5 \mu\text{L}$ . On the left: the impregnation height is  $1 \mu\text{m}$  and the runs were performed on LIS 1. On the right: the impregnation height is  $0.5 \mu\text{m}$  and the runs were performed on LIS 2 and 3.

The tests were then repeated with an impregnation height of  $0.5 \mu\text{m}$ , for LIS 2 and 3: in figure 3.14 right, the results are shown. In the case of LIS 2 the first three runs were done sequentially and the last three the successive day: also in this case the first attempt is the less compatible, and as we can see after a day the drops velocity drops drastically (from  $\sim 12 \text{ mm/s}$  to  $\sim 6 \text{ mm/s}$ ). So in the case of LIS 3 the first 6 runs were performed in the same day to see if the velocity will drop in the same way: as we can see the  $2^{\text{nd}}$ ,  $3^{\text{rd}}$ ,  $4^{\text{th}}$  and  $5^{\text{th}}$  runs are the most compatible (around  $\sim 11 \text{ mm/s}$ ), until the velocity drops drastically in the  $6^{\text{th}}$  attempt. The runs from 6 to 9 were performed in the second day and the ones from 10 to 12 the third day: as we can see the velocity drops at a mean value around  $9 \text{ mm/s}$  and then around  $8 \text{ mm/s}$ , so if we perform measurements on successive days without re-impregnate the LIS we have to take into account that the average velocity is reduced, but within 3 consecutive runs the velocities are compatible.

So the parameters for the experiment will be: impregnation oil fomblin Y lvac 06/6, impregnation height  $0.5 \mu\text{m}$ , water droplets of  $5 \mu\text{L}$ , inclination angle  $30^\circ$ , four different samples.



## Chapter 4

# Experimental Results

The goal of this work is to control the motion of sessile water droplets sliding on an inclined plane through the interaction with the dielectrophoretic force generated by the illumination on the Lithium Niobate. In the next paragraphs we explore this kind of dynamics with different types of illumination (intermittent or continuous), different angles of inclination of the luminous pattern, with a saline solution instead of pure water and different shapes of luminous patterns. These preliminary measurements are necessary to establish some parameters to realize the motion control of sessile droplets on LN samples with different conditions.

In particular, all the next measurements will be performed with an output power set to 943 mW, which corresponds to  $P_{mon}=1.885$  V, to always work in the same initial condition. The power arriving on the sample can be controlled by the motorized goniometer, as we have seen in the previous section. In Figure 4.1, we can see a prototype of the type of measurements acquired in these preliminary studies: the illumination pattern given to the SLM is a rectangular shape 26 mm x 1 mm inclined at a certain angle with respect to the direction of sliding of the droplet and is placed in the middle of its motion, which is highlighted in post-production, since the Basler camera cannot record the green light coming from the sample. To discharge the LN sample and set it for a new measurement, water droplets are pipetted all over the area, and the drops are removed after 15 minutes, to ensure complete discharge. The droplets sliding on the sample are of 5  $\mu$ L of highly pure water.

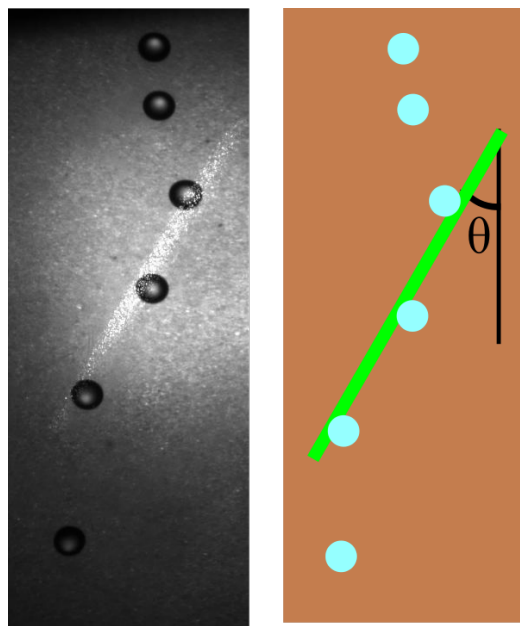


Figure 4.1: Example of the motion of a single droplet on the illumination pattern. The angle of inclination of the pattern is  $\theta$ . The pattern is added on the image in post-production.

## 4.1 Intermittent Illumination

The first kind of explored illumination is the intermittent one: the sample is illuminated for a certain amount of time (shutter open) and then illumination is turned off (shutter closed). As we have seen in the previous section, the power of the laser beam arriving on the sample and the illumination interval time can then be precisely controlled using the motorized goniometer and the electronic shutter.

### 4.1.1 Pendant Drops Fall Height

The first goal is to investigate the charge accumulation due to the illumination of the sample and the different regimes that can occur. To do this the sample, in this case LIS 2, is mounted in horizontal position. The needle is put perpendicular to the sample and at  $\sim 15$  mm. The sample is illuminated for different intervals of time and at two different powers. After the illumination is turned off, a drop of  $2 \mu\text{L}$  is generated on the needle and the sample is moved in a continuous vertical way near the drop until it falls and reaches the sample. The measurement is repeated for six different positions on the substrate. In Figure 4.2 (a-b), we can see the scheme of the mechanism and a representation of the forces acting on the droplet: the capillary force  $F_c$  directed upward, due to the interaction between the needle and the droplet, and the gravitational force  $F_g$  and the dielectrophoretic force  $F_{DEP}$ , due to the interaction with the dielectrophoretic field generated by the LN, both directed downward. When the sample comes close to the droplet, the dielectrophoretic force increases until the result of it plus the gravitational force is greater than the capillary force, and so the droplet falls. From Figure 4.2 (c-d), we can observe that the droplet is attracted to the borders of the illumination pattern, as we expect from the simulations shown in Section 2.5. Sometimes the force is so strong that the droplet is broken into little droplets, all attracted to the borders of the pattern.



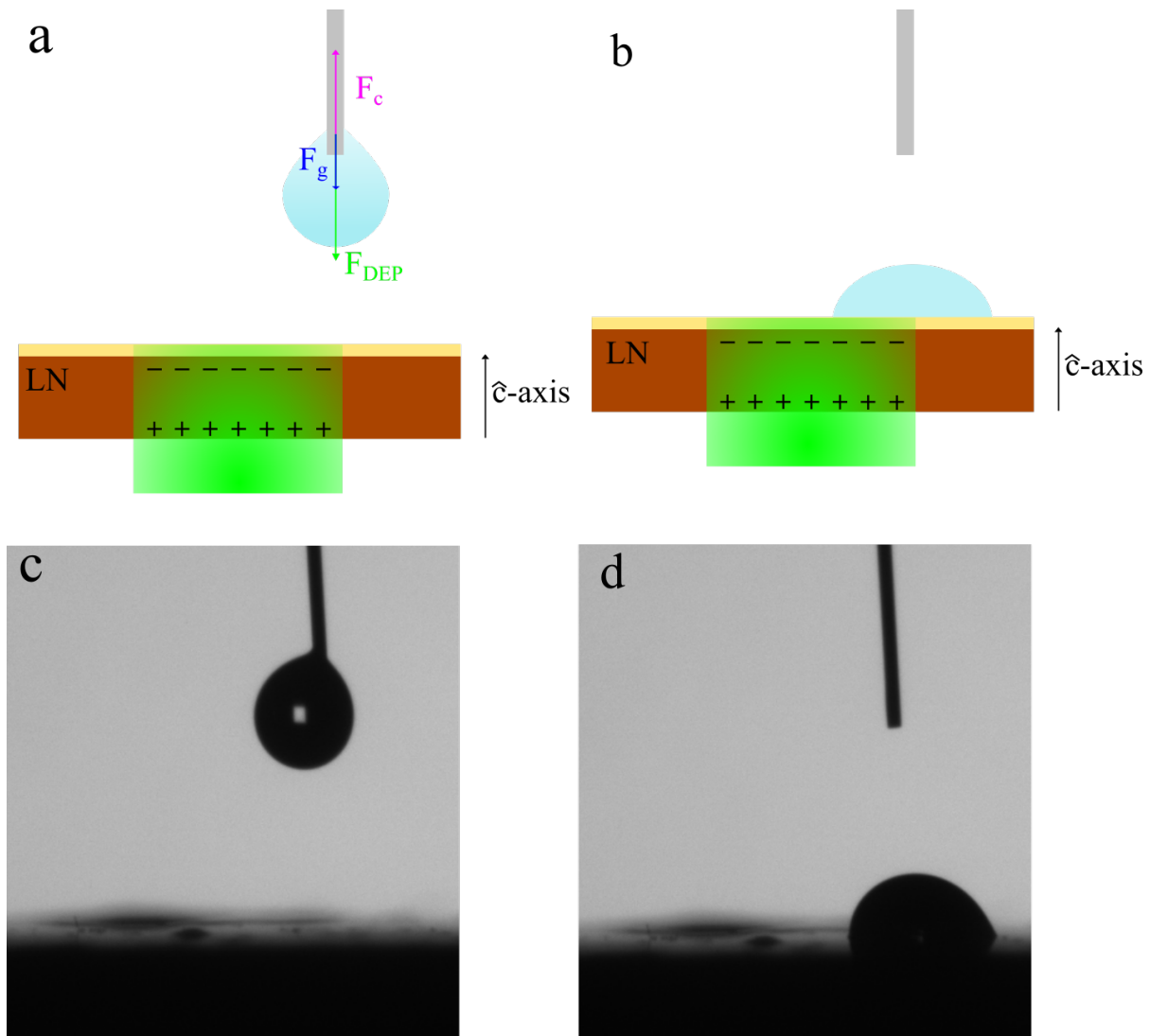


Figure 4.2: Effect of the dielectrophoretic force on the pendant water droplet of  $2 \mu\text{L}$ . The sample is illuminated for 30 s at 50 mW. In figure (a) there is a scheme of the forces acting on the droplet, while (b) shows the fallen droplet attached to the border of the illuminated shape. Figures (c-d) are sequential photos of the droplet falling.

As we can see from Figure 4.3, the height of fall depends on the illumination time and on the power of the laser beam arriving on the sample. We can also distinguish two different regimes (more evidently in the case of 100 mW): in the first part of the graph, before 40 min of illumination, there is a somewhat linear growth of the height of the drop fall, and so of the charge accumulated on the sample. Then the curve changes shape and seems to reach a saturation value. We know that the charge accumulated on LN reaches a value which depends on the light intensity and the exposure time.

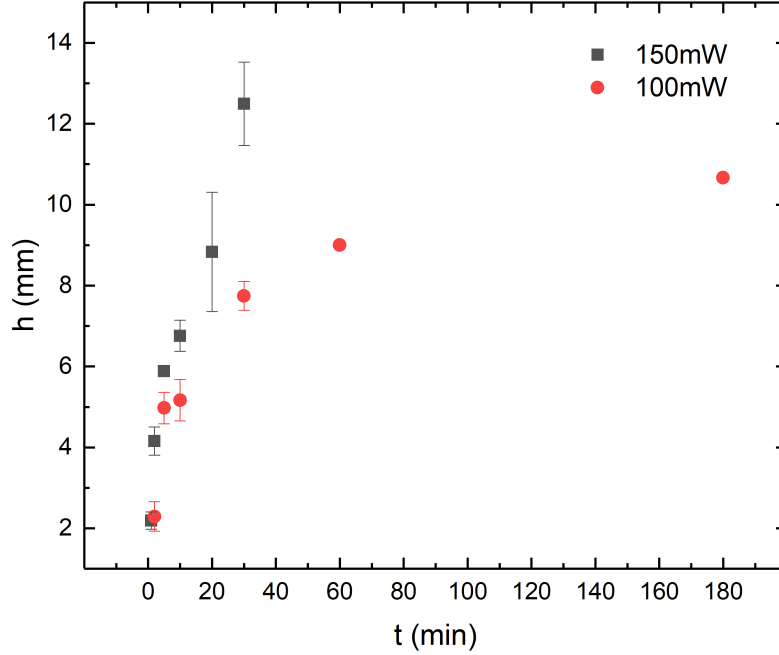


Figure 4.3: Height of fall as a function of the illumination time, for 100 mW and 150 mW.

To perform the various measurements, our first idea was to put the sample always at saturation, so the charges are always the same and we can better confront the results. As we can see from Figure 4.3, the time to reach saturation are of the order of an hour in both cases, and with the optical path of the experimental setup, the maximum power is  $\sim 160$  mW. Accordingly, in the next measurements, we have decided to use maximum illumination intervals of time of the order of one minute for convenience. We are then operating in the "linear" regime of the LN.

#### 4.1.2 Velocity of droplets on the illuminated pattern

From the initial tests of sessile water droplets sliding on the LN substrate illuminated, we have seen that the droplets decelerate when moving along the pattern. We have then compared the speed of the droplets sliding before reaching the pattern and on the pattern. To do this, the sample is tilted by  $30^\circ$  and illuminated for 30 seconds at 50 mW. Then trains of 5 droplets of  $5 \mu\text{L}$  are produced with a rate of  $2 \mu\text{L/s}$  and a delay of 20 seconds between each one. The sliding motion of these trains are recorded and repeated in three different positions of the sample and for LIS 3 and 4. The inclinations of the pattern with respect to the direction of the sliding of the droplets are  $5^\circ$ ,  $30^\circ$  and  $45^\circ$ . In Figure 4.4, the ratio between the two velocities is plotted as a function of the inclination angle of the pattern, where it is defined as

$$\text{Ratio} = \frac{v_{op}}{v_{bp}} \quad \text{where "op" = on pattern, "bp" = before pattern} \quad (4.1)$$

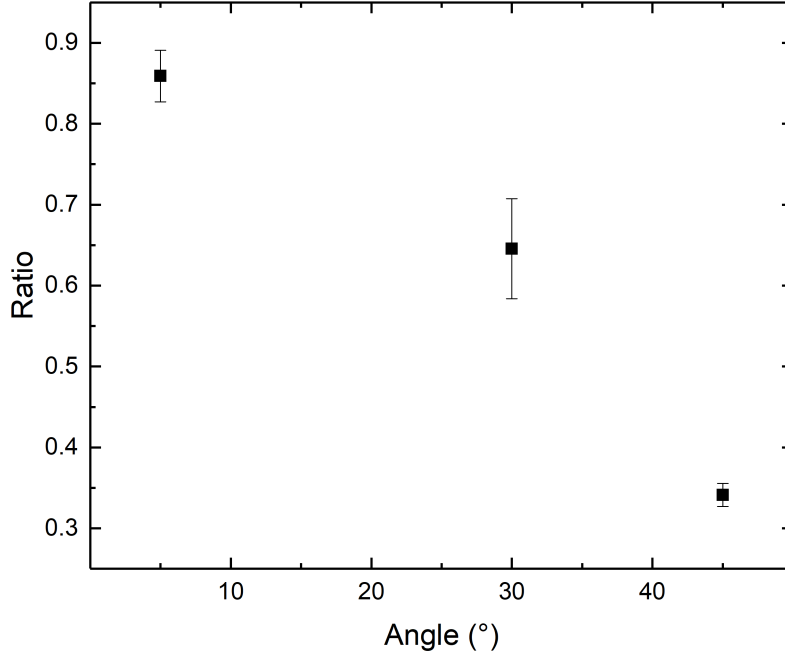


Figure 4.4: Ratio of the velocity of the droplets before the pattern and on the pattern as a function of the angle of inclination of the area illuminated.

After these measurements we find that  $30^\circ$  inclination is a good compromise to see an effective deviation of the motion of the droplet, without a significant decrease of its speed.

### 4.1.3 Natural Discharge of Lithium Niobate

Another measurement to test optowetting behaviour of LN, is to measure the discharge time of the sample due to internal recombination of the charges. To do this, the sample is illuminated with the usual pattern at 50 mW for 30 seconds. Then 20 droplets of  $5 \mu\text{L}$  are let slide on the sample inclined of  $30^\circ$ , with rate  $2 \mu\text{L}/\text{s}$  and a delay of 20 seconds between each one. The droplet first slides down the LIS, then, when it approaches the illuminated area, it is attracted by the dielectrophoretic force on one side of the rectangular stripe, and then it continues its motion down the inclined plane but following the charged area. When the pattern finishes, the droplet goes on sliding down the plane. The droplets are let slide after 30 seconds, 30 minutes and 1 hour after the illumination. The test is repeated in three different positions of the sample, for LIS 1 and 2. In Table 4.1, we report the average value of droplets that follow the pattern, i.e. follow the entire length of it, as a function of the time waited after illumination for LIS 1 and LIS 2.

LIS 1	
Time waited	Droplets following the pattern
30 s	5
30 min	3
60 min	0
LIS 2	
30 s	10
30 min	6
60 min	0

Table 4.1: In table are reported the number of droplets that follow the pattern illuminated for 30 s at 50 mW, after waiting a certain amount of time after the illumination.

As we can see, the pattern is still active after 30 minutes, but it is less effective. This can be associated to the natural discharge of the sample due to internal recombination. The results for LIS 1 and 2 are different, so we have to take it into account when performing the next measurements.

#### 4.1.4 Crossed patterns

The next step is to find the minimum illumination time, such that one single droplet is deviated. To do this we perform some tests at high powers, like 150 mW, 140 mW and 130 mW. We find that the minimum illumination time is 6 seconds for all three powers (below that no droplet is deviated) and the number of deviated droplets varies from 2 to 5. Since the tests on 130 mW are more consistent we have tried to manipulate the motion of the droplet in an active way: we illuminated for 6 seconds the sample with one inclined stripe (left pattern) and we let slide one droplet. After it finishes its motion (around 40 seconds), the sample is illuminated with another stripe (right pattern) equal to the first one but mirrored and shifted such that it crosses the first pattern at the beginning. After the illumination, a second droplet is let slide, but in this case it should follow the second pattern, since it is "more charged" than the first one. The test is repeated for 30 droplets, each one sliding every 50 seconds to ensure no interaction with the precedent one, in three different position of on LIS 3 and LIS 4. Then the same procedure is repeated for 50 mW and 100 mW, with 10 seconds of illumination.

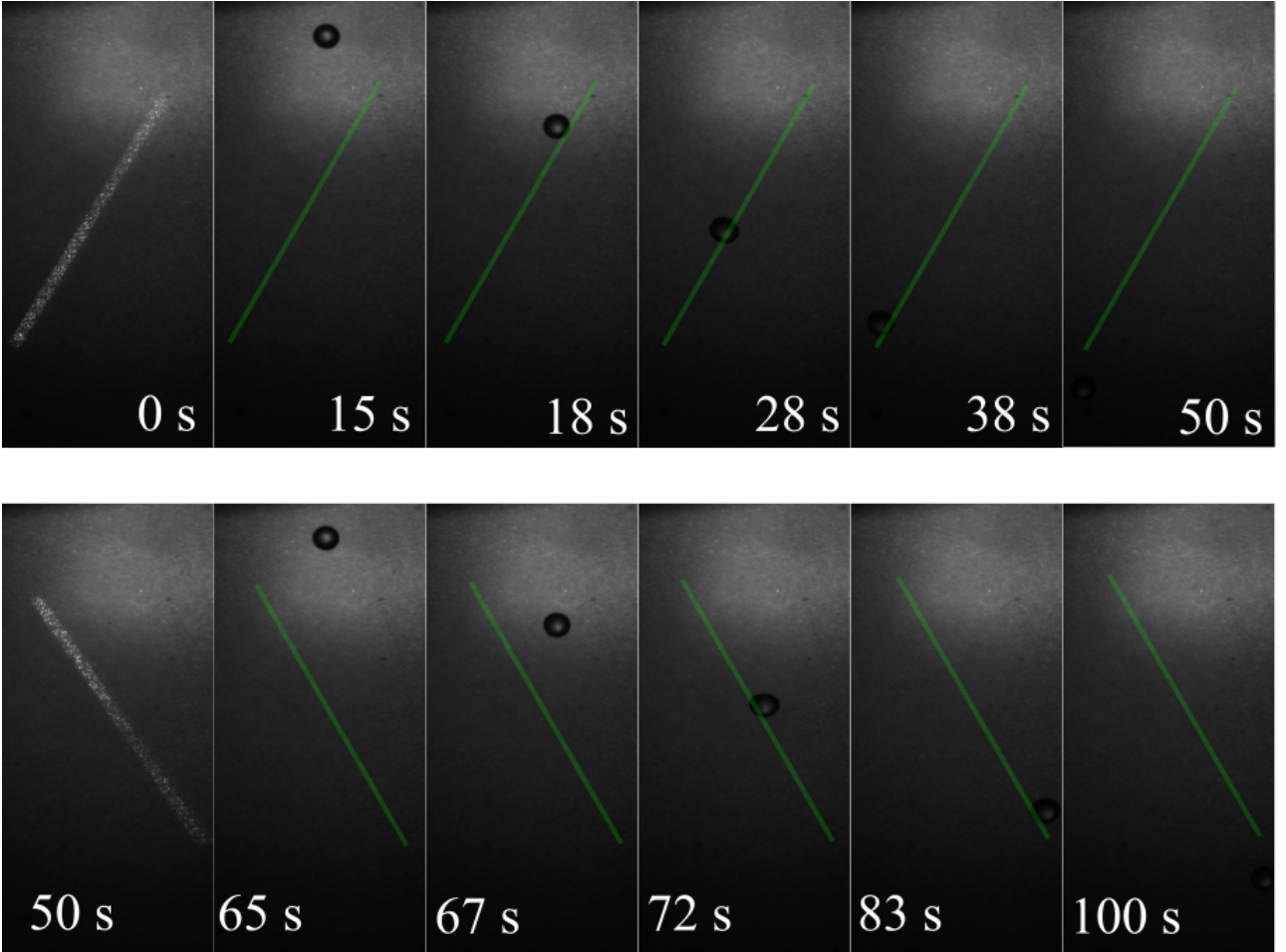


Figure 4.5: Sequence of photos showing the mechanism with crossed patterns: first (0 s) the sample is illuminated for 10 s with the left stripe, then one droplet slides following the illuminated area which is highlighted in green in post-production. When the motion is concluded, the sample is illuminated with the right pattern and another droplet is let slide. This sample is illuminated at 50 mW and this sequence repeated for 30 droplets.

In Table 4.2, we report the number of droplets that go to the left and to the right

Power	Left	Right
130	15	15
100	17	13
50	16	14

Table 4.2: Number of droplets that follow the right and the left pattern on the total of 30 droplets, for three different powers.

This method can be then used to control in an active manner the motion of the droplet to redirect it into two different position (three if we count the sliding without the luminous pattern). The problem with this configuration is the fact that the initial position of the droplet is extremely important to determine with which of the two patterns the droplet will follow: there are cases where two consecutive droplets interact with the same stripe despite the illumination of the mirror one.

We have observed in a fast test that instead of generating a single droplet, a train of five droplets have a better efficiency: the illuminated area is almost discharged by the train and so the next five droplets are interacting unequivocally with the last illuminated area, and so a better control is achieved.

#### 4.1.5 Discharge of the Fe:LiNbO<sub>3</sub> induced by the droplets

In the previous tests we have seen that the sample is illuminated by the laser for a certain amount of time and then if we let slide some droplets on the sample, only a definite amount of them will interact with the pattern, after which the other droplets will no longer feel the dielectrophoretic force. The LN sample charges like a series of capacitors: the first one composed by the LN substrate and the second by the dielectric layer (PTFE filter and oil). After the illumination, the droplets enhance the discharge phenomenon, with respect to the natural recombination of the sample which will take several minutes to hours to discharge completely, depending on the illumination power and time, while when the droplets are let slide it can take minutes or seconds, depending on the frequency of the droplets. A few different hypothesis may explain these observations:

- the droplets may take some charge from the sample charging themselves and discharging the substrate;
- the droplets move the underlying oil and so in this way they move the charges away from the pattern;
- the droplets enhances the local humidity and this favorites the discharge of the sample.

To try to verify the first hypothesis some tests have been carried out. In the first one two symmetric stripes are generated on the sample: one on the right and one on the left, both ending in the same area, distant few millimeters. Two droplets are let slide simultaneously one on the right stripe and one on the left stripe to make them arrive in the same area at the end of the interaction with the pattern. The two droplets will slide along the inclined sample in parallel. We record the motion of these droplets and we look for deviation from sliding motion from the interaction of the two droplets. If a deviation occurs, it may indicate that the two droplets are taking away some charges from the illuminated area. No deviation has been observed in our tests. Another test consists of sliding two droplets in parallel on a illuminated square area. Also in this case no deviation as been seen after the two droplets leave the illuminated area.

Another different test is to put a charged object, made of glass (positive charge) or teflon (negative charge), near the area after the droplets interact with the illuminated area. Since the side of LN sample has negative charges, the droplets should take away them. So they should be attracted by the glass object and rejected by the teflon one. The result instead shows that the droplets are always attracted by the charged object. In conclusion, all these tests suggest that the droplets are not charged after the interaction with the illuminated area. Another test of discharge of the pattern is made using a saline solution of water and KCl, which is the most common in electrowetting experiments. The solution prepared has a concentration of 2M. The sample is illuminated for 20 seconds at 50 mW, and then 20 droplets of 5  $\mu$ L are let slide on the sample and the number of them fully interacting with the pattern is reported. The test is repeated in three different positions of the sample, for water droplets and saline solution droplets, and for LIS 1 and LIS 2. In Table 4.3, the number of droplets interacting with the pattern are reported: as we can see there is no difference between the saline solution and the water droplets in LIS 1, and a slightly difference in LIS 2.

LIS 1					
0 M			2 M		
a	b	c	a	b	c
5	5	5	5	5	6
LIS 2					
a	b	c	a	b	c
9	10	11	12	12	12

Table 4.3: Number of droplets that follow the pattern for droplets of saline solution and water for three different positions (a, b, c) and for LIS 1 and LIS 2. The sample is illuminated for 20 s at 50 mW.

Since the concentration of the saline solution is very high, we expected a remarkable difference between the saline solution and water in the interaction with the pattern, but such difference is not observed. Another difference between the solution and water is that the speed of the saline solution droplets before interacting with the pattern is slightly higher ( $\sim 12\%$ ) with respect to the water droplets. The speed on the pattern is instead the same for both water and saline solutions droplets. So from the data reported there is no evident correlation between the concentration of salt in water and the discharge process of LN sample.

Another test performed on the samples is to repeat the drop height fall measurements but with different conditions. The sample is illuminated for 10 minutes of time and at 100 mW. After the illumination is turned off, 30 seconds are waited, and then a drop of  $2\ \mu\text{L}$  is generated on the needle and the sample is moved in a continuous vertical way near the drop until it falls and reaches the sample. It is found that the droplet falls at  $\sim 10\ \text{mm}$ . The same measure is repeated a second round, but this time a droplet of  $20\ \mu\text{L}$  is put in the illuminated area under the needle: in this way we simulate the way we discharge the sample. After 30 seconds the droplet is removed, the drop of  $2\ \mu\text{L}$  is generated on the needle and the sample is moved near the droplet. As we expect in this case the droplet is not attracted by the sample, and its height fall is approximately zero.

Finally, a sample of LN is covered with Parafilm, a solid, polymeric film with a thickness of  $\sim 130\ \mu\text{m}$ , which is much higher than that of the PTFE filter. The same measurement is repeated, and we find that also in this case the droplet of  $20\ \mu\text{L}$  discharges the sample, since we do not observe any interaction between the pendant droplet and the sample. Therefore, we can exclude that the sliding motion of the droplets induces a displacement of the underlying oil and so a redistribution of the charges. Further experiments are under way to try to understand if the LN discharges through the air humidity locally enhanced by the deposition of the water droplets.

## 4.2 Continuous Illumination

In the previous sub-section we have seen the results with intermittent illumination: the problem with this technique is that only a limited number of droplets can interact with the illuminated pattern before LN sample discharges. The illumination to interact only with a single droplet has not been found and when illuminating at high powers, even with short illumination time, the droplets can exhibit pinning. The other way to use the setup is at continuous illumination. In this way the laser is always on and the only way for LN to be discharged is by interacting with the sliding droplets. The characteristics of this method are that the powers are lower (maximum 50 mW) and the sample is illuminated for a certain amount of time before the droplets are let slide, to ensure that the first one interacts with the illumination stripe. In this section we summarize our study to find the best parameters to ensure the maximum number of droplets interacting with the illumination pattern without pinning, interaction with other droplets or other unexpected effects. First we repeat the measurements with different angles of the illumination pattern, then we try to generate trains of 50 and 100 droplets, and finally different shapes of illumination patterns are tested.

### 4.2.1 Velocity of droplets on the illuminated pattern

Like in the previous sub-section, we have compared the velocity of the droplets before interacting with the illuminated area and on the stripe. In this case we illuminate at 10 mW for 120 seconds to ensure the interaction with the first droplet, and 20 droplets are let slide. The measure is repeated for 6 different angles  $\theta$  of inclination of the illumination pattern with respect to the unperturbed droplet direction:  $5^\circ, 10^\circ, 20^\circ, 30^\circ, 40^\circ, 45^\circ$ , and for two samples LIS 1 and LIS 2. In Figure 4.6, we can see the ratio of the velocity of the droplet on the pattern on the velocity of the droplet before the interaction with the pattern, as a function of the angle of inclination of the pattern.

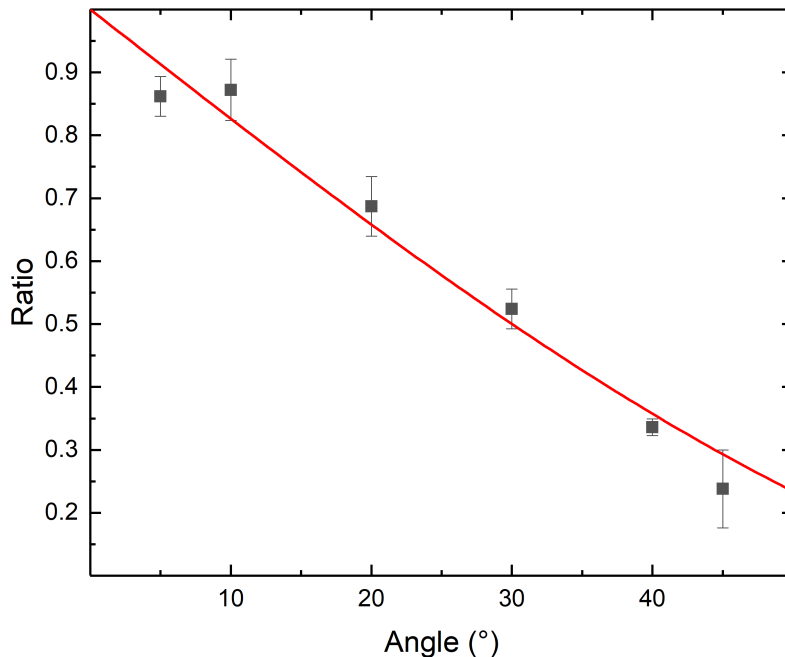


Figure 4.6: Ratio of the velocity of the droplets before the interaction with the stripe and on the illumination pattern as a function of the angle of inclination of the area illuminated. In red the function  $f(x) = 1 - \sin \theta$ .

We can see that the results seem to follow a trend: in the graphic we superimposed the function  $f(x) = 1 - \sin \theta$ , which is compatible with the results of the measurements. We can see that the only measurement not compatible is the one for  $5^\circ$ : we can think at the ideal case when  $\theta$  is  $0^\circ$  the ratio is one, like there is no interaction, but in the real case there will be always some interaction with the pattern and so the ratio will not reach the theoretical value of 1, but a kind of saturation. After performing these measurements, we have decided also in this case to keep the inclination angle of the illuminated stripe of  $30^\circ$ , to see an effective deviation of the motion of the droplet, without a significant decrease of its speed.

### 4.2.2 Train of droplets

The final goal of this experiment is to control a large number of droplets in a robust way, without pinning of droplets on the substrate or interactions between them. We have seen in the previous section that the droplets interacting with the illuminated stripe somewhat discharge the illuminated area. In this section we try to find a compromise between the frequency of droplets sliding on the sample, which discharge the illuminated area, and the laser intensity which charges LN continuously. To do this we change two parameters in the program of the syringe pump: the rate of droplets, which gives a period of time for the generation of the droplet  $t_g$ , and the delay between each droplets generated,  $t_d$ . These two time periods give the frequency of droplets generated per second:

$$f = \frac{1}{t_g + t_d}$$

$t_g$  is 5 s and is constant since the rate is always set at  $2 \mu\text{L/s}$ , while the variable is  $t_d$  which is varied between 1 s and 15 s. The power arriving from the laser beam on the sample is set at: 5 mW, 10 mW, 20 mW and 50 mW. From previous observations we have seen that at high powers with long illumination time periods ( $\sim \text{min}$ ) the dynamics of the droplet becomes unpredictable and pinning phenomena can occur to avoid these problems, the laser power is always kept below 50 mW. Another



parameter is the time of illumination before the droplets train starts: this is the minimum time of illumination such that the first droplets interact with the illuminated area for each power. It is 270 s for 5 mW, 150 s for 10 mW, 50 s for 20 mW and 20 s for 50 mW, which were found from some preliminary tests.

The first measurements involve trains of 50 droplets with  $t_d$  5 s, 10 s and 15 s. In the case of 50 mW, these periods of time are too long and the droplets do not exhibit a constant motion, so  $t_d$  is set at 5 s, 1 s and 0.5 s. Each train is repeated 3 times and all LN samples are used. In Figure 4.7 on the left, we report the efficiency of the train as a function of the frequency of droplets for different powers. The efficiency is defined as the percentage of droplets that follow the illumination pattern without pinning or interaction with other droplets.

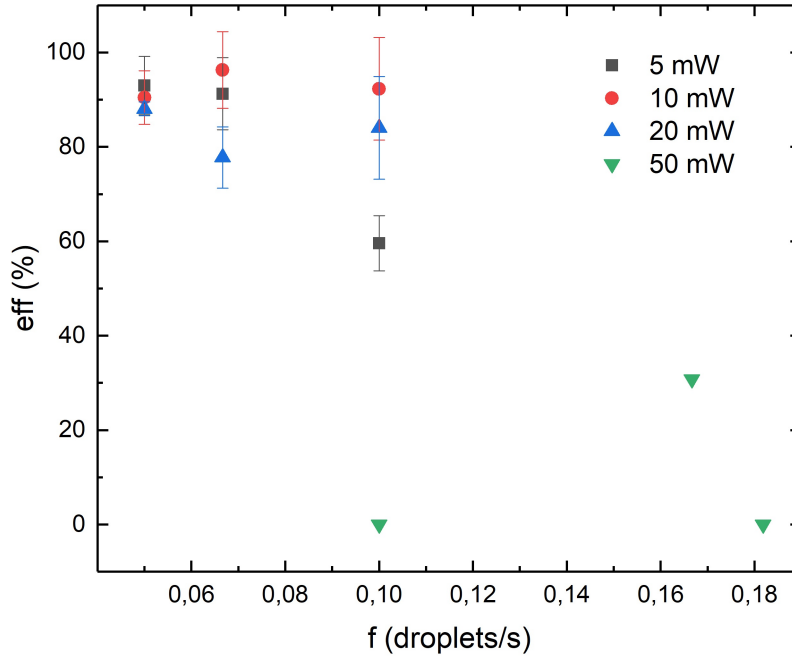


Figure 4.7: The efficiency of the train of 50 droplets as a function of the frequency of droplets for 5 mW, 10 mW, 20 mW and 50 mW.

As we can see the efficiency is really low in the case of 50 mW: the frequency of droplets is not high enough to compensate the fact that the illuminated area is charging continuously: the droplets start to exhibit pinning in different points of the pattern and can continue their motion once they merge with other droplets. In the other cases the efficiency is around 80-85% for all the powers tested. The only point with lower efficiency is the case for 5 mW with  $t_d$  5 s: this due to the fact that the frequency of droplets is too high and the power is not enough to compensate the discharge due to the sliding droplets. Another fact to take into account is that the LIS, and the filter substrate, can still present defects or sites where sometimes a droplet is pinned.

After these preliminary tests with trains of 50 droplets we start to generate trains of 100 droplets. From what we had learnt from the previous measures, the case of 50 mW is discarded, since the results are too unpredictable and unstable to have a robust train. Accordingly, we assign a time delay  $t_d$  of 10 s for 5 mW, 9 s for 10 mW and 7 s for 20 mW. These choices are a consequence of the tests on the 50 droplets trains, and we thought that will lead to the best result, so high efficiency. The measurements are repeated 3 times, using all LN samples. In Figure 4.8 we can see the results for the three different trains.

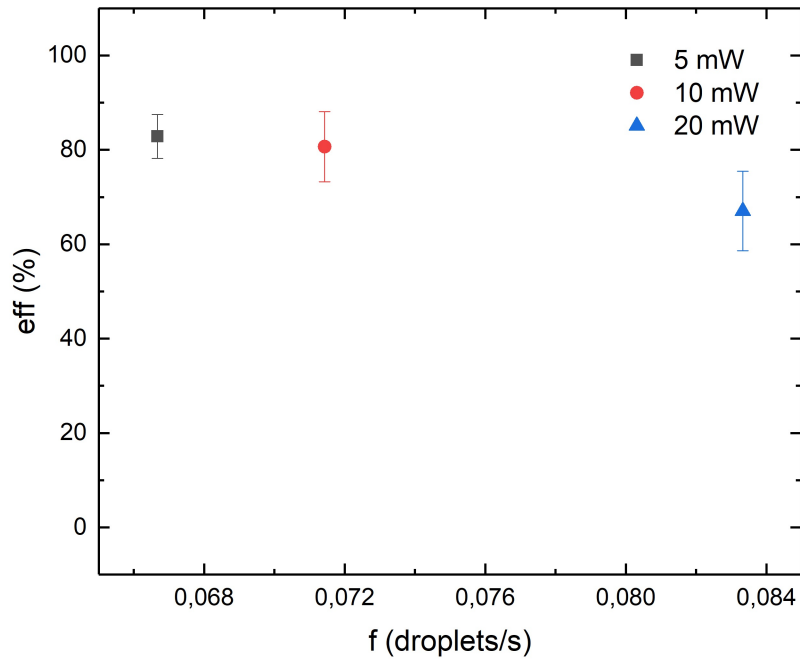


Figure 4.8: The efficiency of the train of 100 droplets as a function of the frequency of droplets for 5 mW, 10 mW and 20 mW.

As we can see the average efficiency is around 80% and so a little less from the previous results. This is due to the fact that the frequency of the droplets is not exactly correct to balance the fact that the sample is continuously charging: the dynamics of the first droplet is very different from the dynamics of the fiftieth or the hundredth. From the video recorded of the droplets we can see that also the shape of the droplets change from the first ones to the final ones, which could be indicative of the different interaction between the droplet and the illumination pattern as the droplets are generated. To compare this different dynamics, we analyse the sliding motion of the first three droplets and that of the final three droplets. In Figure 4.9 we confront the velocity of the droplets before reaching the pattern,  $v_{bp}$ , with the velocity on the pattern,  $v_{op}$ .

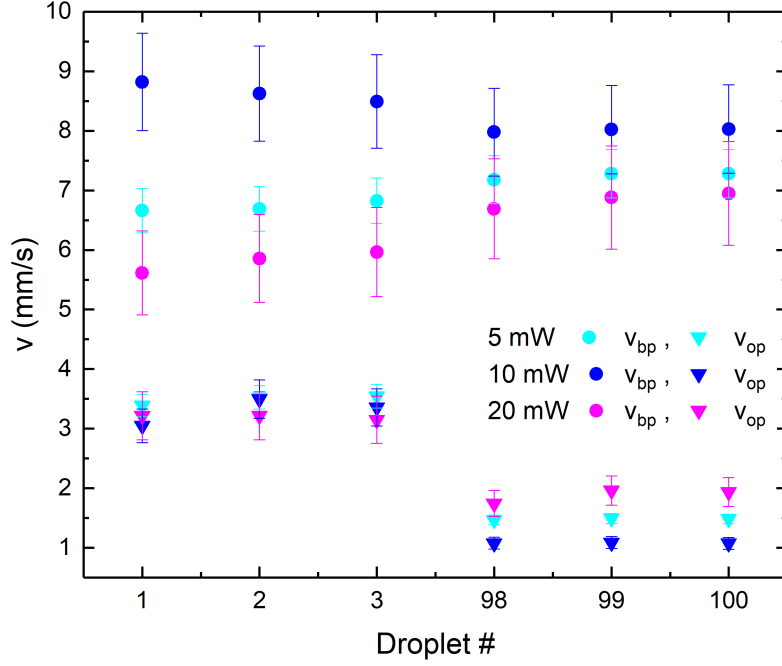


Figure 4.9: The velocity of the first three droplets confronted with the velocity of the last three droplets for different trains (5 mW, 10 mW and 20 mW). The circular symbol is  $v_{bp}$  and the triangular symbol  $v_{op}$ .

As we can see the velocities ( $v_{bp}$  and  $v_{op}$ ) of the first three droplets are compatible for each power, likewise the final three droplets. The velocity of the droplet falls when on the pattern, as we have seen in the previous tests, and for the last three droplets, this fall is higher. This is due to the fact that after 100 droplets the overall charge of the pattern is increasing and thus the interaction between the droplet and the illuminated area. We can see also that the velocity of the last three droplets  $v_{bp}$  is decreasing, with respect to the first three, in the case of 10 mW, and increasing in the case of 5 mW and 20 mW. Since the droplet is attracted by the dielectrophoretic force by the illuminated area, the reason of the velocity increase can be attributed to the increase of charges in the illuminated area, instead the opposite when the velocity is decreasing. The fact that the cases are different depends on  $t_d$ : in the case of 5 mW and 20 mW  $t_d$  is too high to prevent the accumulation of charges over time, instead in the case of 10 mW  $t_d$  is too low and the droplets are discharging the pattern over time. The efficiency of the train can be then improved by adjusting the frequency of the droplets to reach a perfect balance between charge and discharge of the LN sample.

### 4.2.3 Different patterns of illumination

After achieving train of droplets with a good efficiency, some new shapes of the pattern are tested, to see if the motion of the droplet can be controlled in a more complex way. These patterns have the same area of the rectangular shape and are illuminated at 10 mW. The first test is performed with a curved shape, and each droplet is generated with  $t_d$  of 20 s. In Figure 4.10 we can see a series of sequential photos of a droplet following the illumination pattern.

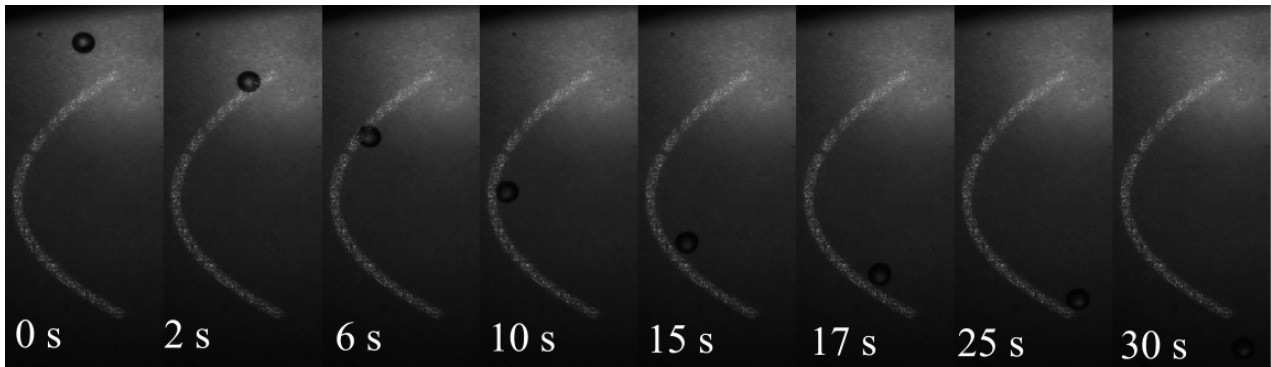


Figure 4.10: Sequential photos of the motion of a droplet on the curved pattern. The pattern on the images is add in post-production.

In the sequence of images of 4.10 ,the droplet is the last one of its train and we can see that is perfectly following the optical pattern. In the case of the first droplets the motion is not so smooth and in the curved region the droplet tends to jump from one side to another.

The second pattern tested is a rectangular line broken in three parts: the first one has  $30^\circ$  of inclination, the second one is vertical and the last one has  $30^\circ$  of inclination but in the other direction. In this case  $t_d$  is 9 s. In Figure 4.11 we can see a series of sequential photos of two droplets following the illumination pattern.

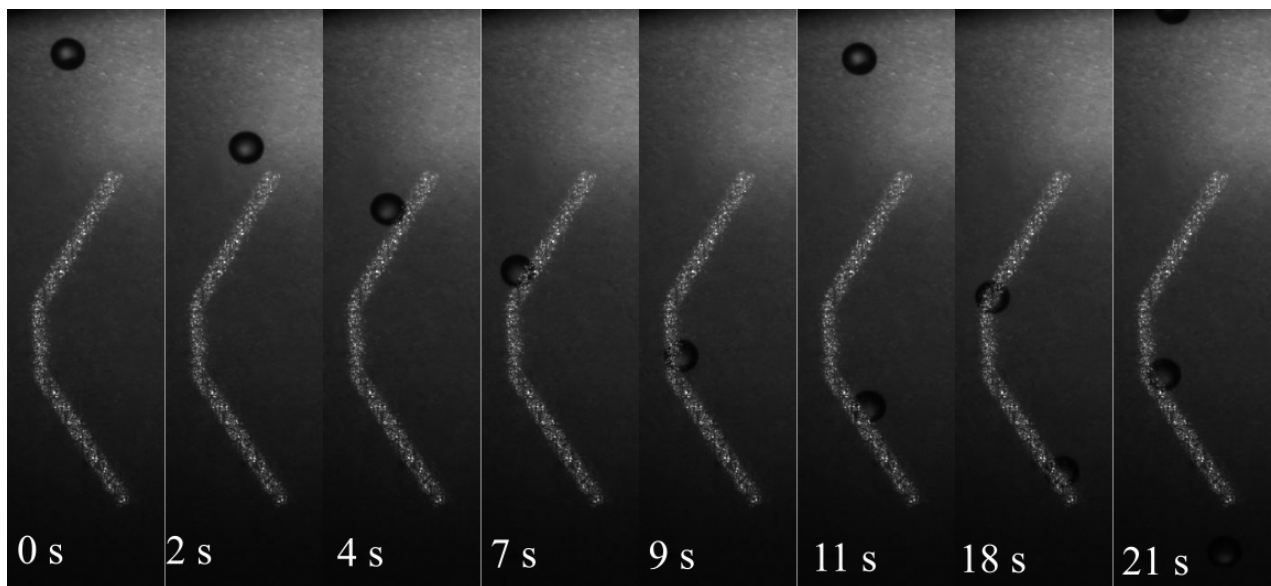


Figure 4.11: Series of sequential photos of the motion of two droplet on the broken pattern. The pattern on the images is add in post-production.

In this case the central zone has more edges, which tend to attract the droplet. The complete motion is not uniform because it accelerates towards the edges.

The last pattern is an undulated shape with three different curvatures. In this case  $t_d$  is 25 s. In Figure 4.12 we can see a series of sequential photos of one droplet following the illumination pattern.

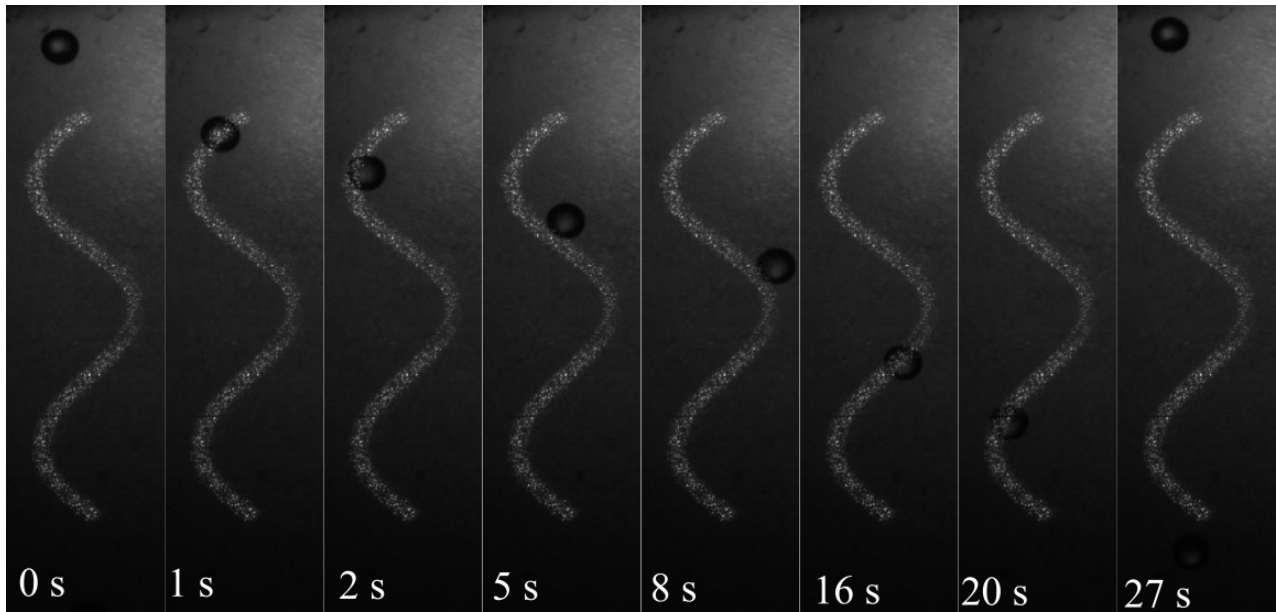


Figure 4.12: Sequential photos of the motion of a droplet on the undulated pattern with three curves. The pattern on the images is add in post-production.

Also in this case the motion shown in the sequence is of one of the last droplets. Like in the first alternative pattern, the motion of the droplet evolves from a irregular motion into a smooth one, where the droplet follows continuously the pattern.

The trains of 20 droplets generated for all the three patterns have all efficiency 100%. With these more complicated patterns it has to be taken into account also the effect of the shape of it and the evolution of the motion of the droplets, as the illuminated area is charging.



## Chapter 5

# Conclusions

This work of thesis deals with the manipulation of sessile water droplets by exploiting the photovoltaic effect exhibited by Lithium Niobate (LN) crystals. To facilitate the motion of micro-liter droplets, the LN crystal is coated with a lubricant impregnated surface. In this way, the droplets can slide due to gravity even at inclination angles of the crystals as low as  $5^\circ$ . The motion of droplets on such engineered surfaces has been studied by illuminating the LN crystal with a laser turned on either continuously or intermittently. The resulting dielectrophoretic force due to the photoinduced charge is analyzed by moving a pendant drop with respect to the laser spot and observing its deformation. Furthermore, the motion of gravity driven droplets in presence of illuminated stripes of different shapes produced with a surface light modulator has been analyzed for different light intensities, exposure times and droplets frequencies. A first result of this preliminary exploration is that trains of tens of droplets can follow the illuminated stripe in a reliable way, a clear indication that it is possible to guide their motion by light without the use of metallic electrodes connected to power supplies. For a wider application of this novel methodology, it is necessary to overcome the discharge of the LN crystals after the passage of drops. Our preliminary tests carried out in this work tend to exclude that this is due to either a charging of the droplets or a displacement of the charge due to the lubricant motion. Further studies are under way to see whether it occurs through the surrounding air, whose humidity is enhanced by the passage of drops. Once this issue has been solved, we are confident that the motion of droplets can be accurately and easily controlled with light on our engineered surfaces.





# Bibliography

- [1] P.-G. De Gennes, F. Brochard-Wyart, and D. Quéré, *Capillarity and wetting phenomena: drops, bubbles, pearls, waves*. Springer Science & Business Media, 2013.
- [2] N. Le Grand, A. Daerr, and L. Limat, “Shape and motion of drops sliding down an inclined plane,” *Journal of Fluid Mechanics*, vol. 541, p. 293, 2005.
- [3] K.-Y. Law and H. Zhao, *Surface wetting: characterization, contact angle, and fundamentals*. Springer International Publishing Basel, Switzerland, 2016.
- [4] G. Mistura and M. Pierno, “Drop mobility on chemically heterogeneous and lubricant-impregnated surfaces,” *Advances in Physics: X*, vol. 2, no. 3, pp. 591–607, 2017.
- [5] A. Lafuma and D. Quéré, “Slippery pre-suffused surfaces,” *EPL (Europhysics Letters)*, vol. 96, no. 5, p. 56 001, 2011.
- [6] J. D. Smith, R. Dhiman, S. Anand, E. Reza-Garduno, R. E. Cohen, G. H. McKinley, and K. K. Varanasi, “Droplet mobility on lubricant-impregnated surfaces,” *Soft Matter*, vol. 9, no. 6, pp. 1772–1780, 2013.
- [7] S. Nishimoto and B. Bhushan, “Bioinspired self-cleaning surfaces with superhydrophobicity, superoleophobicity, and superhydrophilicity,” *Rsc Advances*, vol. 3, no. 3, pp. 671–690, 2013.
- [8] H. F. Bohn and W. Federle, “Insect aquaplaning: Nepenthes pitcher plants capture prey with the peristome, a fully wettable water-lubricated anisotropic surface,” *Proceedings of the National Academy of Sciences*, vol. 101, no. 39, pp. 14 138–14 143, 2004.
- [9] A. Eifert, D. Paulssen, S. N. Varanakkottu, T. Baier, and S. Hardt, “Simple fabrication of robust water-repellent surfaces with low contact-angle hysteresis based on impregnation,” *Advanced Materials Interfaces*, vol. 1, no. 3, p. 1 300 138, 2014.
- [10] S. Anand, A. T. Paxson, R. Dhiman, J. D. Smith, and K. K. Varanasi, “Enhanced condensation on lubricant-impregnated nanotextured surfaces,” *ACS nano*, vol. 6, no. 11, pp. 10 122–10 129, 2012.
- [11] M. J. Kreder, J. Alvarenga, P. Kim, and J. Aizenberg, “Design of anti-icing surfaces: Smooth, textured or slippery?” *Nature Reviews Materials*, vol. 1, no. 1, pp. 1–15, 2016.
- [12] A. K. Epstein, T.-S. Wong, R. A. Belisle, E. M. Boggs, and J. Aizenberg, “Liquid-infused structured surfaces with exceptional anti-biofouling performance,” *Proceedings of the National Academy of Sciences*, vol. 109, no. 33, pp. 13 182–13 187, 2012.
- [13] B. Berge, “Electrocapillarité et mouillage de films isolants par l’eau,” *Comptes rendus de l’Académie des sciences. Série 2, Mécanique, Physique, Chimie, Sciences de l’univers, Sciences de la Terre*, vol. 317, no. 2, pp. 157–163, 1993.
- [14] F. Mugele and J.-C. Baret, “Electrowetting: From basics to applications,” *Journal of physics: condensed matter*, vol. 17, no. 28, R705, 2005.
- [15] C. Hao, Y. Liu, X. Chen, Y. He, Q. Li, K. Li, and Z. Wang, “Electrowetting on liquid-infused film (ewolf): Complete reversibility and controlled droplet oscillation suppression for fast optical imaging,” *Scientific reports*, vol. 4, no. 1, pp. 1–7, 2014.
- [16] T. Volk and M. Wöhlecke, *Lithium niobate: defects, photorefraction and ferroelectric switching*. Springer Science & Business Media, 2008, vol. 115.
- [17] R. Weis and T. Gaylord, “Lithium niobate: Summary of physical properties and crystal structure,” *Applied Physics A*, vol. 37, no. 4, pp. 191–203, 1985.

- 
- [18] S. Grilli and P. Ferraro, “Dielectrophoretic trapping of suspended particles by selective pyroelectric effect in lithium niobate crystals,” *Applied Physics Letters*, vol. 92, no. 23, p. 232 902, 2008.
- [19] M. Luennemann, U. Hartwig, G. Panotopoulos, and K. Buse, “Electrooptic properties of lithium niobate crystals for extremely high external electric fields,” *Applied Physics B*, vol. 76, no. 4, pp. 403–406, 2003.
- [20] U. Schlarb and K. Betzler, “Refractive indices of lithium niobate as a function of wavelength and composition,” *Journal of applied physics*, vol. 73, no. 7, pp. 3472–3476, 1993.
- [21] A. Glass, D. v. d. Linde, and T. Negran, “High-voltage bulk photovoltaic effect and the photorefractive process in linbo3,” in *Landmark Papers On Photorefractive Nonlinear Optics*, World Scientific, 1995, pp. 371–373.
- [22] K. Peithmann, A. Wiebrock, and K. Buse, “Photorefractive properties of highly-doped lithium niobate crystals in the visible and near-infrared,” *Applied Physics B*, vol. 68, no. 5, pp. 777–784, 1999.
- [23] M. Carrascosa, A. Garcia-Cabañes, M. Jubera, J. Ramiro, and F. Agulló-López, “Linbo3: A photovoltaic substrate for massive parallel manipulation and patterning of nano-objects,” *Applied Physics Reviews*, vol. 2, no. 4, p. 040 605, 2015.
- [24] L. Chen, S. Li, B. Fan, W. Yan, D. Wang, L. Shi, H. Chen, D. Ban, and S. Sun, “Dielectrophoretic behaviours of microdroplet sandwiched between In substrates,” *Scientific reports*, vol. 6, no. 1, pp. 1–10, 2016.
- [25] C. Sebastián-Vicente, E. Muñoz-Cortés, A. Garcia-Cabañes, F. Agulló-López, and M. Carrascosa, “Real-time operation of photovoltaic optoelectronic tweezers: New strategies for massive nano-object manipulation and reconfigurable patterning,” *Particle & Particle Systems Characterization*, vol. 36, no. 9, p. 1 900 233, 2019.
- [26] J. F. Muñoz-Martinez, J. B. Ramiro, Á. Alcázar, Á. Garcia-Cabañes, and M. Carrascosa, “Electrophoretic versus dielectrophoretic nanoparticle patterning using optoelectronic tweezers,” *Physical Review Applied*, vol. 7, no. 6, p. 064 027, 2017.
- [27] T. Jones, “Electromechanics of particlescambridge univ,” *Press, Cambridge*, 1995.
- [28] J. F. Muñoz-Martinez, Á. Alcázar, and M. Carrascosa, “Time evolution of photovoltaic fields generated by arbitrary light patterns in z-cut linbo 3: Fe: Application to optoelectronic nanoparticle manipulation,” *Optics Express*, vol. 28, no. 12, pp. 18 085–18 102, 2020.
- [29] A. Puerto, A. Méndez, L. Arizmendi, A. Garcia-Cabañes, and M. Carrascosa, “Optoelectronic manipulation, trapping, splitting, and merging of water droplets and aqueous biodroplets based on the bulk photovoltaic effect,” *Physical Review Applied*, vol. 14, no. 2, p. 024 046, 2020.
- [30] H. P. K.K. (). “Hamamatsu opto-semiconductor handboo, k, chapter 12:294-307, 2014,” [Online]. Available: <https://www.hamamatsu-news.de/hamamatsu%20optosemiconductor%20handbook/298/>.
- [31] C. J. Brinker, “Dip coating,” in *Chemical Solution Deposition of Functional Oxide Thin Films*, Springer, 2013, pp. 233–261.